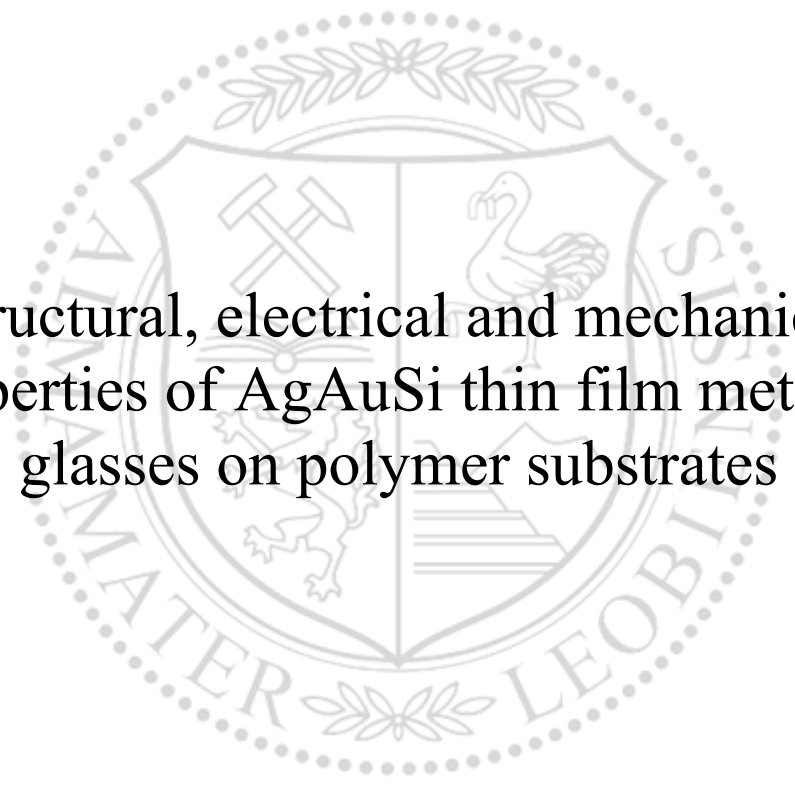Chair of Functional Materials and Materials Systems

Master's Thesis

Structural, electrical and mechanical properties of AgAuSi thin film metallic glasses on polymer substrates

Lisa-Marie Weniger, BSc

May 2021

EIDESSTATTLICHE ERKLÄRUNG

Ich erkläre an Eides statt, dass ich diese Arbeit selbständig verfasst, andere als die angegebenen Quellen und Hilfsmittel nicht benutzt, und mich auch sonst keiner unerlaubten Hilfsmittel bedient habe.

Ich erkläre, dass ich die Richtlinien des Senats der Montanuniversität Leoben zu "Gute wissenschaftliche Praxis" gelesen, verstanden und befolgt habe.

Weiters erkläre ich, dass die elektronische und gedruckte Version der eingereichten wissenschaftlichen Abschlussarbeit formal und inhaltlich identisch sind.

Datum 18.05.2021

Unterschrift Verfasser/in
Lisa-Marie Weniger

Acknowledgements

Abstract

English

In this thesis, the structural, electrical and mechanical properties of $Ag_xAu_{85-x}Si_{15}$ thin film metallic glasses (TFMGs) on polymer substrates were investigated. The films were fabricated by magnetron sputter deposition from three elemental targets, which allowed to systematically vary the composition and film thickness. In contrast to crystalline metals, where the electrical resistivity increases with decreasing film thickness, AgAuSi TFMGs were found to have a decreasing electrical resistance with decreasing film thickness. Additionally, ultrathin TFMGs with a thickness of 12 nm exhibited superior mechanical properties that were linked to the suppression of shear bands, where no material damage occurred after straining the films up to 10%. In cyclic bending tests, AgAuSi TFMGs outperformed crystalline metals due to their high elastic straining limit. The combination of these remarkable properties makes AgAuSi TFMGs possible candidates for future materials in flexible electronics.

Deutsch

Im Zuge dieser Arbeit wurden die strukturellen, elektrischen und mechanischen Eigenschaften von dünnen $Ag_xAu_{85-x}Si_{15}$ metallischen Gläsern (TFMGs) auf Polymersubstraten ermittelt. Die Filme wurden mittels Magnetronsputterverfahren von drei Einzelelement-Targets hergestellt, was systematische Variation der Schichtzusammensetzung und Schichtdicke erlaubte. Im Gegensatz zu kristallinen Metallen, wo die elektrische Leitfähigkeit dünner Schichten mit abnehmender Schichtdicke zunimmt, wurde in AgAuSi TFMGs eine mit kleiner werdender Schichtdicke abnehmende elektrische Leitfähigkeit gemessen. Ultradünne TFMGs mit einer Schichtdicke von 12 nm wiesen herausragende mechanische Eigenschaften auf, die mit der Unterdrückung von Scherbändern verknüpft werden konnte. In Zugversuchen wurde keine Materialschädigung bei Dehnungen von bis zu 10% gemessen. In zyklischen Biegeversuchen übertrafen AgAuSi TFMGs kristalline Metalle aufgrund ihrer hohen elastischen Dehnbarkeit. Die Kombination dieser herausragenden Eigenschaften macht AgAuSi TFMGs zu einem möglichen Kandidaten für Materialien für zukünftige flexible Elektronik.

Table of contents

1. Introduction

With the miniaturization of flexible electronic based systems, the materials used approach limits defined by the underlying physics. The electrical resistivity of conventional crystalline thin film materials drastically increases with decreasing thickness [1][2]. However, in order to further miniaturize high-performance electronics, a low electrical resistivity of e.g. interconnect lines is crucial. A novel group of materials, thin film metallic glasses (TFMGs), exhibits a constant electrical resistivity over its thickness. Furthermore, TFMG alloy systems reveal superior mechanical behavior, which could enable reliable and long-lasting flexible electronics [3].

Within this thesis, a TFMG alloy system comprised of Au, Ag and Si will be further developed. Au is of natural interest due to its low electrical resistivity, high thermal conductivity and high corrosion resistance. Ag is chemically very similar and therefore fully miscible with Au. Ag is further known as the best metallic conductor and possesses antimicrobial properties [4][5]. These properties make it a promising constituent for substituting in part for the Au in AuSi metallic glasses. Moreover, as the Ag price lies well below the Au price, a partial replacement of Au by Ag makes the novel alloy system more affordable. To gain comprehensive knowledge about this system, AgAuSi thin films are grown by unbalanced magnetron co-sputter deposition from three elemental targets. This approach allows to systematically vary the composition of the thin films and thereby understand the compositional influence on mechanical and electrical properties as well as tune and optimize the system towards highest performance and stability. Subsequently, the films are characterized with respect to their atomistic structure, stability as well as mechanical and electrical properties. The applied methods are X-ray diffraction, transmission electron microscopy, differential scanning calorimetry, resistivity measurements, tensile straining, cyclic bending tests and post-mortem scanning electron microscopy.

The aim of this thesis is to gain fundamental knowledge of AgAuSi TFMGs and to identify alloying compositions that could possibly enable applications like ultrathin conductive layers, semi-transparent flexible electrodes, chemically inert implantable electrodes as well as mechanically robust diffusion barriers.

2. Theory

Within this work, the structural, electrical, and mechanical properties of AgAuSi TFMGs on polymer substrates are investigated. For the interpretation and understanding of this complex composite material system, first a brief introduction to metallic glasses (MGs) in general will be given, then the main properties of TFMGs will be overviewed followed by the description of the state-of the-art regarding noble-metal based MGs.

2.1 Metallic glasses

Metallic glasses are metallic alloys with an amorphous ("glassy") structure. They can be fabricated by fast quenching and undercooling a liquid, by severe plastic deformation of a solid, or by vapor-state methods [6]. Vapor-state methods are only used for the synthesis of thin films. Here, the most prominent vapor-state method is physical vapor deposition (PVD), which will be described in more detail later.

2.1.1 Thermodynamics of metallic glasses

MGs are non-equilibrium materials, consequently, equilibrium or near-equilibrium fabrication routes cannot be applied. For the production of MGs, the glass forming ability is crucial. It indicates whether a melt tends to solidify in the amorphous or crystalline state. A good glass forming ability means that the amorphous structure is easily obtained. Certain alloy compositions are associated with good glass forming abilities, which are commonly known as Inoue criteria [7]:

- The alloy should be composed of at least three different elements. The glass forming ability increases with the number of elements.
- The atomic size differences should at least be 12%.
- The alloy must have a negative heat of mixing.

Additionally, it was observed, that glasses are usually easily formed for compositions near deep eutectics [8].

For a better understanding of the thermodynamic behavior of MGs, the processes occurring when quenching an MG from a melt will be discussed. When a melt is cooled underneath its crystallization temperature, two opposing mechanisms happen simultaneously. One is crystallization, where the driving force increases with decreasing temperature. The other mechanisms is based on the increasing viscosity with decreasing temperature, that slows down diffusion and therefore diminishes crystallization [9]. If the liquid is quenched fast enough, kinetic arrest will occur, where the viscosity is so high, that no crystallization can occur anymore [7][8]. Fig. 1 (a) demonstrates this behavior in an isothermal transformation

diagram, where the crystallization regime as well as the liquid regime are depicted. Two cooling lines are marked in this diagram. Line 1 represents a slow cooling, where crystallization occurs. Line 2 shows the minimal cooling rate for the fabrication of an MG. To circumvent crystallization, the liquid must be quenched with at least this cooling rate [8]. The enthalpy during the quenching process as a function of material temperature is shown in Fig. 1 (b). As soon as the temperature is lower than the melting temperature T_m, the crystalline phase has the lowest enthalpy possible for that alloy. However, if the material is quenched too fast to crystallize, the melt will be supercooled, and MGs are formed. The kink in the supercooled melt enthalpy line indicates the glass transition at the so-called glass transition temperature T_g. Depending on the cooling rate, different states of MGs can be obtained. The faster the melt is quenched, the less time is available for atomic rearrangement within the MG. This leads to a higher enthalpy of the obtained MG and to a higher T_g [7].
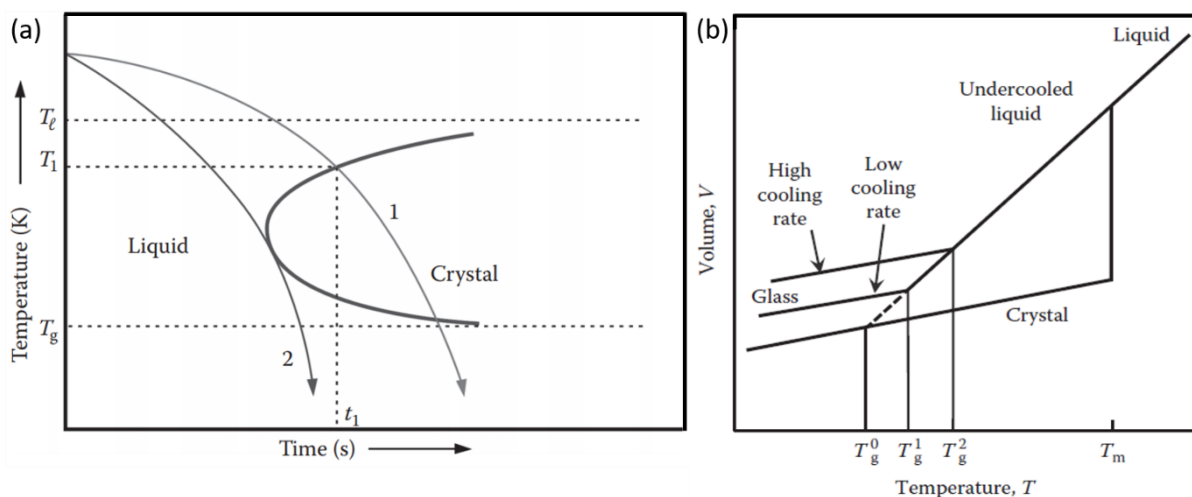
Fig. 1: (a) The isothermal transformation diagram shows the crystalline regime, that needs to be circumvented in order to obtain an MG. The minimal cooling rate therefor is indicated by line 2 [8]. (b): The enthalpy as function of temperature for an MG and a crystal. The faster the MG is cooled, the higher is its enthalpy and T_g [7].

As the crystalline state has a lower energy than the amorphous state, the material will crystallize once it has enough energy to overcome the energy barrier for crystallization. The temperature, where crystallization occurs is called the crystallization temperature T_x. Fig. 2 shows the material behavior upon heating in a graph where the exothermic heat flow is plotted over the temperature. At T_g, the heat flow decreases, indicating that the glass

transition is an endothermic process. Between T_g and T_x lies the supercooled liquid region ΔT_x, where homogeneous flow occurs. The large exothermic peak indicates T_x.
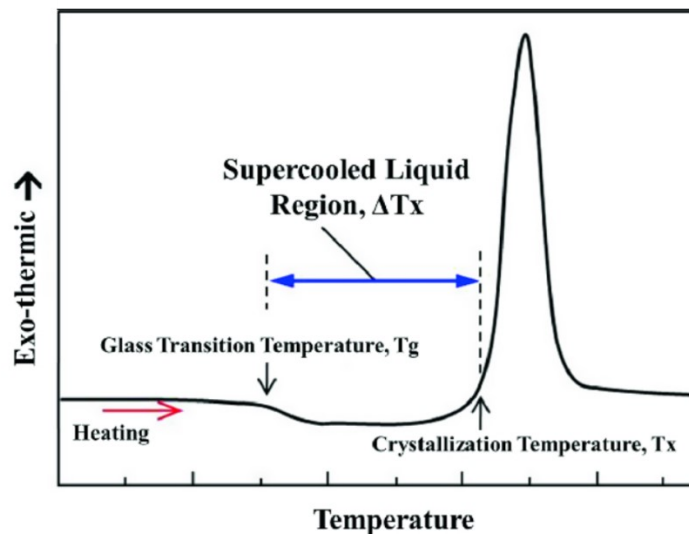
Fig 2.: Exothermic heat flow as a function of temperature for the heating process of an MG, where the glass transition temperature T_g, the supercooled liquid region ΔT_x and the crystallization temperature T_x can be seen [10].

2.1.2 Atomistic structure of metallic glasses

The amorphous structure can be compared to the structure of fluids. In contrast to crystals, they do not exhibit a long-range order. However, the structure of MGs can be described by a short-range and a medium-range order. The short-range order describes the nearest neighbors of an atom, as well as their distance and bonding angle, whereas the medium-range order represents clusters of atoms [11].

The structure of MGs is often displayed using the radial distribution function (RDF) or the pair distribution function (PDF). They can be easily converted into each other and are therefore not discussed individually [11]. The RDF shows the number of atoms that can be found surrounding a centered atom as a function of the distance from the centered atom. Therefore, it can be used to estimate coordination numbers and atomic neighbor distances. The RDF is measured in diffraction experiments. Fig. 3 shows atoms in an amorphous structure and a corresponding RDF diagram [12]. A centered atom is marked red, and the circles around the centered atom mark the nearest (green atoms) and next-nearest (yellow atoms) neighbors of that atom. The first peak in the RDF indicates the atoms in the first shell around the centered atom, and the second peak the second shell of atoms. After that, the RDF converges to a steady value, which corroborates the lack of a long-range order in MGs.
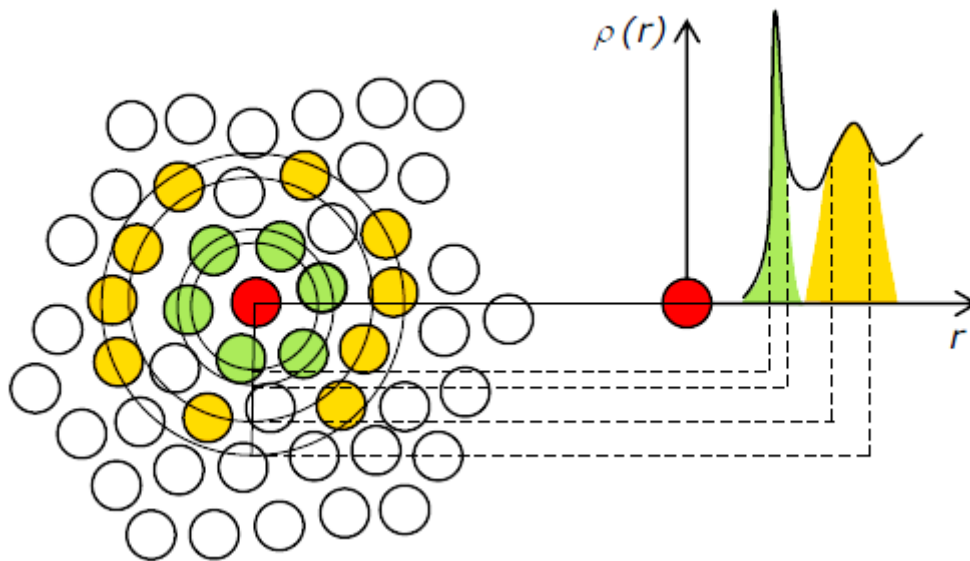
Fig. 3: Atoms in amorphous structure with a corresponding RDF. The nearest and next-nearest neighbors of a centered atom are displayed in color [12]*.*

It should be pointed out that the RDF provides one-dimensional information of a three-dimensional structure and is therefore only correct for isotropic materials. However, even with the knowledge of the average atomic distances and their frequencies in isotropic MGs, the exact atomic structure remains unknown. Thus, many models for the atomic structure of MGs, that can explain different properties of the materials, have been proposed.

One of the first approaches was the random densely packed hard sphere model (DPHS) proposed by Bernal [13] for liquids. There, the atoms are represented by non-deformable spheres, that are densely packed together in polyhedrons, with tetrahedrons and octahedrons accounting for the vast majority of atom structures. Several authors have demonstrated, that the PDF obtained for the DPHS model are in good agreement with experimentally obtained RDF [14][15].

A widely spread approach is the free volume theory, that is based on the DPHS model suggested by Bernal. In MGs, the atoms are typically not as densely packed as in crystals of the same composition. The additional space between the atoms in MGs is called free volume [7][8][16]. It is created, when the atoms within a material do not have enough time to rearrange while cooling. Depending on the cooling rate, different amounts of free volume can be obtained for the same compositions. In general, higher cooling rates result in higher amounts of free volume [17]. Material properties like self-diffusion and deformation behavior strongly depend on the free volume, as they all involve atomic jumps, that are facilitated by large free volumes [16]. Although the free volume model in combination with

the DPHS model does provide insight in the atomic structure of MGs and can explain many aspects, certain inconsistencies, especially with metal-metalloid MGs exist. For example, for an atomic jump in a liquid, a free volume of approximately 80% of the volume of an atom is required for the atom to jump to that place. However, in metallic liquids, this value is about 10%. This indicates, that liquid metals cannot be treated like other liquids, and molecular dynamic simulations suggest, that diffusion happens not only over single atomic jumps, but over chain processes, where multiple atoms are involved [8].

Multiple newer models were proposed, in order to overcome these discrepancies. A promising model is the model proposed by Miracle, where clusters of atoms are densely packed in face-centered cubic structures. This model can well explain the short-range order and the medium-range order of MGs. The short-range order is determined by the clusters, and the medium-range order by the connection between the clusters. Internal strains prohibit the cluster packing over more than a few clusters, and are therefore the reason for the lack of long-range order in MGs [18]. Another model was designed to fit the PDF obtained by neutron scattering at different temperatures. The tight-bond-cluster model describes randomly distributed clusters, that are similar to the atoms in the DPHS model. They are interconnected by bonds, that are strongly temperature dependent, and therefore can explain the different behavior of MGs at different temperatures. As the clusters are randomly distributed, free volume like areas exist between them, where the atoms are assumed to behave like in the supercooled liquid region [19][20]. Both the tight-bond-cluster model and Miracle's model can elegantly describe both short-range and medium-range order. However, for both models, further research is necessary to investigate, whether they can also sufficiently describe the mechanical behavior of MGs [11].

2.1.3 Characteristic properties of metallic glasses

The reason for the growing interest in MGs lies in their unique properties, the most important ones being high corrosion resistance, high strength, and a high elastic limit, which leads to exceptional fatigue behavior and high elastic energy storage. The corrosion resistance results from the homogeneity of MGs. In crystalline materials, damage in passive layers often occurs at grain boundaries, precipitates, or dislocations. As these structures are not present in amorphous alloys, superior corrosion behavior can be found. Therefore, MGs are of special interest as protective coatings [7][10]. For good fatigue behavior, high strength and a high elastic limit are needed, which are both provided by MGs. Usually, MGs have an elastic straining limit of about 2%, compared to a typical value of 0.5% in most crystalline metals and alloys [10][21]. Their strength is relatively high, especially in compression [22]. The deformation behavior of MGs strongly depends on temperature. Beneath T_g, MGs exhibit a brittle-like behavior, especially under tensile strain [23], manifested by catastrophic

fracture immediately when the elastic limit is reached. Above T_g, in the supercooled liquid regime, homogeneous flow can be observed for low strain rates [23]. In contrast to crystalline materials, that can deform plastically due to mechanisms like dislocation gliding, twinning or grain boundary sliding, the only known deformation mechanism in MGs beneath glass transition is the formation of shear bands [24][23]. There, plastic deformation occurs localized, with typical band widths of 20 nm. Shear bands commonly occur at an angle of 45° to the direction of the applied stress and can propagate through the whole material causing brittle material failure [23].

2.2 Thin film metallic glasses

TFMGs on polymer substrates combine the superior mechanical and chemical properties of MGs with the flexibility offered by a supporting thin polymer layer. These films are conventionally synthesized using vapor deposition methods. PVD methods, as the deposition method used for the samples investigated in this thesis, represent non-equilibrium processes, where MGs are easily obtained for wide compositional ranges. Also, thin films are ideal for glass forming, as only minor energy amounts are applied to the films during relatively short deposition durations.

2.2.1 Mechanical properties

Metallic glasses exhibit interesting size effects in their mechanical properties. Contrary to the brittle-like behavior of bulk MGs (BMGs), pronounced plastic deformation can be observed for MGs in small dimensions. A breakthrough in those size effects was described by Guo in 2007, where samples with dimensions of 100 nm $\times$ 100 nm $\times$ 250 nm elongated 25% under tensile strain with neck formation [25]. These results implicate the possible application of MGs in microdevices or thin films. Although TFMGs are only restricted in one dimension, promising size effects can be observed as well.

Before the onset of size effects, TFMGs show mechanical properties that are comparable to BMGs, with an elastic straining limit of about 2% followed by brittle-like failure. The mechanical properties of TFMGs on polymer substrates can then be described by the shear lag model. It is frequently used for mechanical properties of composite materials consisting of a brittle component and a ductile or highly elastic component under tensile strain. According to the shear lag model, the brittle films fail due to cracks perpendicular to the straining direction [26]. This is also true for TFMGs, where the cracks reach through the entire film thickness as well as through the whole width of the sample. Additionally to these cracks, the formation of shear bands can be observed in TFMGs. In contrast to BMGs, where typically one shear band leads to material failure, the support provided by the polymer prohibits catastrophic failure in TFMGs. Therefore, the formation of multiple shear bands as

well as the interactions between shear bands and cracks can be observed in TFMGs on polymer substrates.

For ultrathin (<10 nm) films, crack-free deformation of up to 6% strain was observed [27]. The cracks occurring at strains higher than 6% were isolated cracks with small dimensions that had lengths in the order of 100 nm, which did not cause catastrophic material failure at tests with a maximum applied strain of 10%. These extraordinary results can be explained by the suppression of shear bands. Molecular dynamic simulation suggests that shear bands need sample dimensions in the range of 10 - 20 nm to fully develop and become critical [28]. These results make ultrathin TFMGs promising candidates for applications where they are exposed to cyclic loads.

2.2.2 Electrical properties

TFMGs typically have resistivity values in the range between 100 and 200 μΩcm [29][30], i.e. about two order of magnitudes higher than pure crystalline metals. However, as the film thickness declines, the resistivity of crystalline metals drastically increases. Crystalline metals typically exhibit electron mean free paths in the order of a few tens of nanometers [31]. As soon as the film thickness reaches similar dimensions, the resistivity of the material increases drastically, which is caused by an increased scattering of electrons at the grain boundaries and at the external surface of the material [2][32]. For example, the electron mean free path of Au at room temperature is 37.7 nm [31]. Fig. 4 depicts the resistivity of Au as function of the film thickness. The resistivity starts to increase at a thickness of around 40 nm, i.e. at the thickness reaching the size of the electron mean free path. At around 20 nm, which is half the magnitude of the electron mean free path, the resistivity of Au increases rapidly. When extrapolating this rapid resistivity increase, the resistivity of Au will be higher than the resistivity of an MG at around 10 nm. In MGs, the electron mean free path is in the order of a few nm [33]. Therefore, even very small film thicknesses in the range of 10 nm do not influence the resistivity, which is a key factor for electronics of decreasing dimensions.
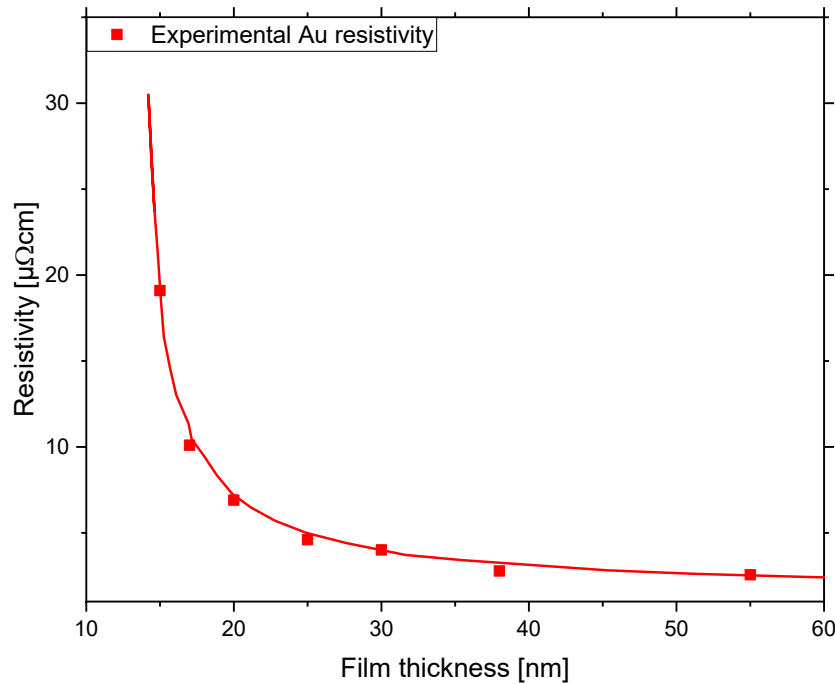
Fig. 4: Resistivity of Au as a function of the film thickness. A dramatic increase of resistivity occurs for film thicknesses smaller than the electron mean free path (redrawn after [2]*).*

2.3 Gold-based metallic glasses

Au is of natural interest due to its low electrical resistivity, high thermal conductivity and high corrosion resistance. The first metallic glasses apart from ultrathin films were AuSi metallic glasses, that were reported by Klement in 1960 [34]. They had a Si content of 25 at%. Experiments with different Si contents revealed a wide amorphous composition range between 20 at% and 80 at% for vapor deposited AuSi TFMGs. However, these films were unstable at room temperature, and crystallization occurred for some films as fast as after 24 h.

Different Au-based MGs were investigated since, in many of them, Cu, Ag and Pd were added to stabilize the AuSi MG. One characteristic of Au-based MGs is a very low T_g, and in many cases also a large supercooled liquid region. For different material compositions, a T_g between 70°C and 130°C was measured, and the ΔT_x ranged between 20 and 60°C. Both properties suggest Au based MGs to be good glass formers and to have a good formability (now in the sense of shape transformability) [35][36][37]. T_g was found to be lower for higher Au contents, and higher if more than two additional elements were used to stabilize the AuSi system [35][36]. High-energy X-ray diffraction and extended X-ray absorption fine structure measurements suggest that the low glass transition temperature in AuCuSi BMGs may be linked to their high packing density [37].

9

Au-based BMGs have high hardness values of about 360 HV, which is about twice the value for crystalline alloys with the same Au content [35]. Systematical studies of the $Au_xSi_{17}Cu_{75.5-x}Ag_{7.5}$ system with x ranging between 40 and 70 revealed that higher Au contents result in lower hardness as well as lower Young's modulus and lower compressive stress. These changes in mechanical properties were also linked to the decreasing T_g with increasing Au content.

The resistivity of $Au_xSi_{17}Cu_{75.5-x}Ag_{7.5}$ varied between 126 and 187 µΩcm and increased with increasing Au content. The obtained values are typical for MGs, which commonly have resistivities between 100 and 200 µΩcm. As higher Au contents lead to lower Cu contents, the almost linear dependence of the resistivity is of no surprise [36].

2.4 Synthesis of thin film metallic glasses by magnetron sputter deposition

For the synthesis of MGs, high cooling rates are essential. Therefore, TFMGs are usually fabricated by PVD methods [6]. There, a solid material source is converted into a vapor phase, which then condenses and nucleates on a substrate [38][39][40]. PVD methods can be divided into thermal evaporation and sputter deposition. In thermal evaporation, a heat source provides the energy for evaporating the material. In contrast, in sputter deposition the atoms in the vapor phase obtained their energy from the momentum transfer that occurs when energetic particles bombard the surface of the material source.

As the fabrication of the samples for this thesis was performed by magnetron sputter deposition, the principles of sputter deposition and followingly magnetron sputter deposition will be described in more detail. A typical sputter deposition setup as depicted in Fig. 5 (a) consists of the material source, the so-called target, and a substrate. They are positioned face to face to each other within a vacuum chamber, where a low pressure of Ar is implemented. By applying a high voltage between target and substrate, the Ar atoms are ionized according to equation (1).

$$Ar + e \rightarrow Ar^+ + 2e^- \quad (1)$$
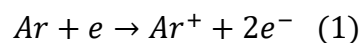
The Ar^+ ions are accelerated by the electric potential towards the cathode, i.e. the negatively charged target. When the incident Ar^+ ions collide with the target, energy is transferred to the near-surface target atoms. If the transferred energy is sufficiently high, this impact leads to a collision cascade within the target, where multiple atoms are displaced from their equilibrium lattice sites. Eventually, surface atoms are ejected (sputtered) from the target. The sputtering process is schematically visualized in Fig. 5 (b).
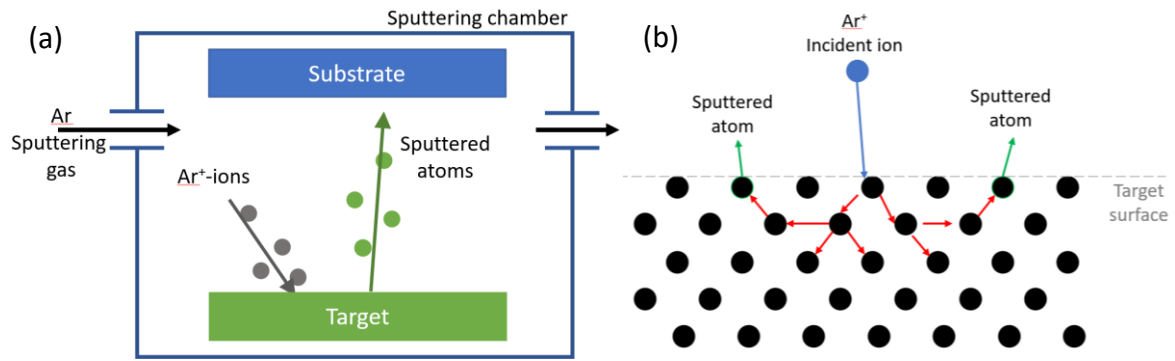
Fig. 5: (a) A typical sputter deposition setup consisting of a target, that is bombarded by Ar⁺ ions, and a substrate, that is coated with sputtered atoms. (b) When the surface of the target gets hit by an incident ion, a collision cascade leads to the displacement of multiple atoms and eventually to the ejection of surface atoms (redrawn after [39]*).*

Magnetron sputter deposition is the predominant sputtering technique and provides higher sputter rates than setups without magnetrons. In magnetron sputter deposition, a magnetic field is established above the target. Fig. 6 shows a planar target with a permanent magnet assembly beneath in (a) side view and (b) top view. The magnetic field lines radially spread from the center of the target to its rims. Due to the Lorentz force, electrons are forced onto a circular path perpendicular to the magnetic field lines. This results in a significantly higher electron concentration near the target. Ar atoms are now very efficiently ionized by collision with electrons as indicated in equation (1).
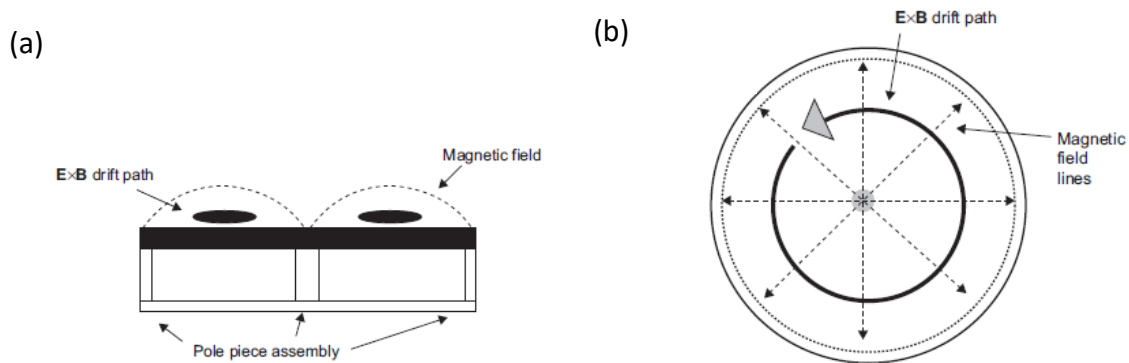
Fig. 6: In magnetron sputter deposition, permanent magnets are placed beneath the target to cause a magnetic field. (a) In the side view, the magnetic field lines are visualized. (b) The top view depicts the circular drift path of electrons [39]*.*

The higher Ar⁺ ion concentration above the target results in an intensified target bombardment rate, and therefore in a higher sputtering rate. It also enables the process to take place at lower pressures and with lower voltages applied to the target [41]. Additionally, as the plasma is confined to the target, the substrate is less bombarded by electrons. This leads to lower substrate temperatures, allowing deposition on materials with

low temperature tolerance like polymers [40]. However, a disadvantage of this configuration is the inefficiency of the target material utilization. The locally restricted electron path (see Fig. 6 (b)) causes a locally increased sputtering rate. As a consequence, the material erosion mainly takes place within circular erosion tracks on the target's surface. After about 10-30% target utilization, the erosion tracks reach through the whole thickness of the target, and the target needs to be replaced. For industrial scales, this inefficiency can be overcome by moving permanent magnets or cylindrical, rotatable target geometries, which allow a material utilization of up to 80% [42].

In magnetron sputter deposition, balanced and unbalanced magnetrons can be distinguished. In a balanced magnetron, the field strength of the outer magnets is as high as that of the inner magnet. Consequently, all field lines pass through the inner magnet. The plasma is then confined closely to the target, which can be a disadvantage, as ion bombardment of the substrate can be desired to enhance the thin film properties [40]. As a solution, unbalanced magnets can be implemented. In this case, the magnetic field lines are not closed, in particular when applying stronger outer magnets some of them stray towards the substrate, also allowing a higher plasma density close to the substrate.

Sputter-deposition is a non-equilibrium process, meaning that the films do not grow according to the thermodynamical equilibrium conditions. In the literature, the microstructure of the growing films is often described by structure-zone-models (SZM) as a function of the homologous temperature of the growing film [40][43]. At higher temperatures, the adatoms have higher energies resulting in enhanced surface diffusion and the ability to migrate to low-energy surface sites [44]. Multiple adaptations of SZM were proposed over the past decades, where also other parameters like the pressure of the sputtering gas or the energy introduced to the growing film, e.g. by applying a bias to the substrate are considered. Here, a brief explanation of the SZMs as function of the homologous temperature as illustrated in Fig. 7 will be given. Typically, four zones are distinguished in the SZM. In the first zone, at homologous temperatures below 0.2, the adatoms have a low mobility. In this zone, porous, columnar films can be observed. The next zone is called zone T or transition zone, and ranges from a homologous temperature of 0.2 to 0.4. Within this zone, the diffusivity of the atoms is already higher than in zone 1, and the characteristic film growth in zone T are V-shaped grains. Then, in zone 2 at homologous temperatures between 0.4 and 0.8, the atoms possess a relatively high diffusivity, and the microstructure typically composes of long, straight columns through the film thickness. Lastly, in zone 3 at homologous temperatures higher than 0.8, recrystallization occurs, and the films possess equiaxed grains. SZMs represent useful guides for the design of crystalline structures, however, as amorphous thin films only recently came into broader interest, no

SZM exists exclusively for them. As metallic glasses need high cooling rates and conditions far from thermodynamical equilibrium for their formation, they are not expected to form in zones of high homologous temperatures.
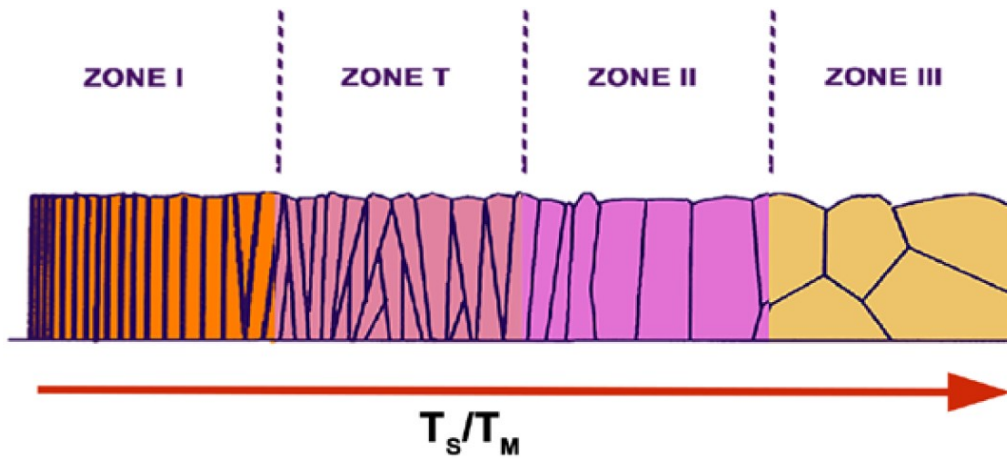

Fig. 7: SZM for film growth in sputter deposition. Zone 1: columnar, porous grains; zone T: V-shaped grains, zone 2: columnar grains; zone 3: equiaxed, recrystallized grains [45].

3. Methods

Within this thesis, AuAgSi TFMGs were fabricated and their microstructure, chemical composition as well as electrical and mechanical properties were investigated. The structure was studied by time-dependent X-ray diffraction (XRD), differential scanning calorimetry (DSC) and transmission electron microscopy (TEM). The chemical composition was analyzed with energy-dispersive X-ray spectroscopy (EDX). Electrical properties were measured by the van-der-Pauw method and the mechanical properties were investigated using tensile tests with in-situ resistance measurements as well as cyclic bending tests. After mechanical testing, post-mortem scanning electron microscopy (SEM) characterization was conducted in order to investigate the failure modes within the samples.

3.1 Film fabrication

Substrate preparation

Different substrate materials were coated for different experiments. For the mechanical tests, 50×50 mm² UPILEX® polyimide (PI) substrates with a thickness of 50 μm were used, whereas for XRD measurements silicon (Si) substrates with dimensions of 7×20 mm² and a thickness of 350 μm were used. For the DSC measurements, 10×10 mm² NaCl substrates were coated. The PI and Si substrates were cleaned for 10 minutes in an ultrasonic ethanol bath. Afterwards, the substrates were blow-dried and directly secured onto the substrate holder using Kapton tape.

Deposition parameters

The thin films were fabricated by magnetron co-sputter deposition as explained in chapter 2.4. The purities of the targets were 99.98% for Au, 99.99% for Ag and 99.999% for Si. The target-to-sample distance was 40 mm. After mounting the sample mask to the substrate holder, the deposition chamber was evacuated to a pressure lower than $1 \cdot 10^{-5}$ mbar. Prior to film deposition, the samples were sputter-etched using an asymmetrically bipolar pulsed direct current (dc) bias voltage of -350 V at a frequency of 50 kHz and a reverse time of 500 μs in an Ar atmosphere with an Ar flow of 200 sccm and a pressure of 10^{-2} mbar. The films were deposited in a non-reactive Ar atmosphere with an Ar flow of 30 sccm corresponding to a pressure of 10^{-3} mbar without external heating and without applying a substrate potential. To achieve different film compositions, the dc power applied to the targets (target area of ~20 cm²) was varied between 6 and 46 W for Au, between 5 and 37 W for Ag, and the power at the Si target was kept constant at 100 W. Different film thicknesses were realized by varying the deposition time between 15 s and 20 min.

3.2 Film thickness and chemical composition

Film thickness

The thickness of the films was estimated from the sputtering rates of the single targets and verified by different measurements methods for different film thicknesses. Using a Zeiss Leo 1525 SEM, cross section thickness measurements were performed on 1000 nm and 500 nm thick films, and the 25 nm and 12 nm thick samples were measured by X-ray reflectivity (XRR) on a Rigaku SmartLab diffractometer.

Chemical composition

The chemical composition was analyzed with EDX in a Zeiss Leo 1525 SEM using a Bruker Quantax system on 500 nm thick films. A measurement voltage of 10 kV was applied, and every sample was measured at least three times at different sample positions for statistical reasons as well as for verifying the homogeneity of the coating. EDX spectra were quantified using Esprit 2.2 software according to internal elemental standards.

3.2 Structural properties

X-ray diffraction

The amorphous state of the films was evaluated using XRD. In preliminary experiments performed for this thesis, optical alterations occurred in AuSi TFMGs. To further investigate whether this was caused by microstructural changes within the films, XRD measurements were repeated after certain time intervals. The first measurement was performed on the same day as the thin film deposition, followed by measurements after 24 h, after one week and after eight weeks and after eight months. The measurements were performed using a Bruker-AXS D8 Advance diffractometer with CuKα radiation using the films deposited on Si substrates. The θ-2θ scans were performed with θ ranging between 20° and 85°, and a step size of 0.02°. The applied voltage was 40 kV, and the current was 40 mA.

Differential scanning calorimetry

Differential scanning calorimetry measurements were performed to investigate T_g, T_x and ΔT_x of AgAuSi TFMGs. As AuSi and AgSi proved to be crystalline in XRD measurements, no DSC measurements were performed on them. DSC experiments were carried out on a Mettler Toledo DSC 3+ under Ar protective gas flow of 50 ml/min and active LN_2 cooling with constant heating rates of 10 K/min using platinum crucibles. The free-standing films were produced by depositing on NaCl substrates and floating the films off in deionized water. In order to provide good thermal contact between the film and the crucible, a sapphire plate was put on top of the sample. For baseline correction, the empty platinum crucibles with the

sapphire plate were measured with the same DSC method and subtracted from the DSC signal.

Transmission electron microscopy

High resolution TEM (HRTEM) micrographs and selected area diffractogram (SAD) patterns were taken with a JEOL 2200FS microscope operated at 200 kV. The diffraction patterns were obtained using a selected area aperture with a diameter of 150 nm. Samples for TEM investigations were obtained by depositing 25 nm thin AgAuSi TFMGs with Ag contents between 10% and 70% directly on ultrathin TEM support grids (3 nm thick carbon, Pelco).

3.3 Electrical properties

The electrical properties were measured using the van der Pauw method on coated PI substrates [46]. With this method, the sheet resistance of thin films or samples of arbitrary shape and unknown size can be measured. The measurement method provides accurate results under the following conditions: four contacts need to be attached to the corners of the sample; these contacts must be small compared to the sample size; the film must be homogeneous and interconnected. During the measurement, a current is applied between two neighboring contacts, and the voltage between the other two contacts is measured. Then, the resistance is calculated from the voltage and the current, and the measurement geometry is changed systematically, so that the current and voltage contacts were applied and measured at every two neighboring contacts. Fig. 8 shows the eight resulting measurement geometries.
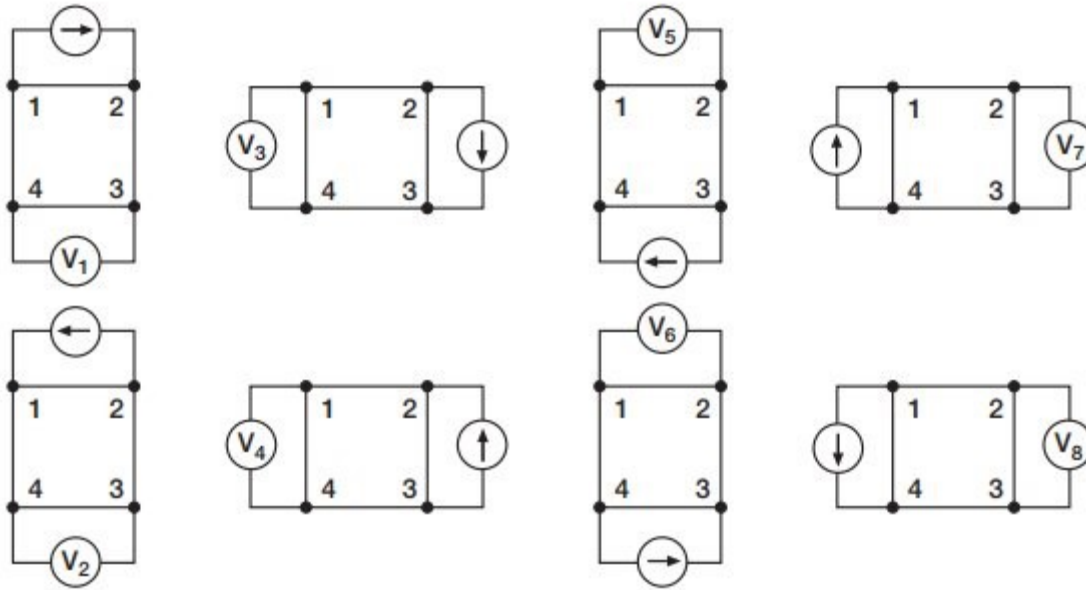
Fig. 8: For van der Pauw measurements, eight different measurement geometries are applied. The contacts 1-4 are marked by dots, the current direction is indicated by an arrow, and the voltage measurements are numbered with V1 to V2 [47].

Next, the average of the resistances obtained by V1, V2, V5 and V6 (see Fig. 8), called R_a, and the average of resistances obtained by V3, V4, V7, and V8, called R_b, are calculated. With these averaged resistances, the sheet resistance can be described using the equation (2):

$$1 = e^{\frac{-\pi \cdot R_a}{x}} + e^{\frac{-\pi \cdot R_b}{x}} \quad \rightarrow \quad y = e^{\frac{-\pi \cdot R_a}{x}} + e^{\frac{-\pi \cdot R_b}{x}} - 1 \quad (2)$$

This equation can be solved graphically, where the function value y at the variable value x=0 equals the sheet resistance. To obtain the resistivity, the sheet resistance needs to be multiplied by the film thickness.

Additionally, the resistivity values obtained by van der Pauw method were compared to 4-point resistivity values measured on a Jandel RM2 4-point probe.

3.4 Mechanical properties

Tensile test

Monotonic uniaxial tensile tests were performed using an MTS Tytron 250 universal tensile tester in displacement-controlled mode. The electric resistance was measured in-situ during straining in 4-point geometry with the electrical contacts incorporated directly in the grips attached to the samples. Samples with a size of 40·4 mm² were cut from 50×50 mm² PI foils

using a scalpel. The initial gauge length amounted to 20 mm. The samples were strained by 10% with a displacement rate of 2.5 μm, which corresponds to a strain rate of 2.5·10^{-4}.

Bending test

For investigating the fatigue behavior of AgAuSi TFMGs, cyclic bending tests were performed on a custom-made bending device called flex-e-test [48]. The flex-e-test consists of a rotatable wheel with grips, onto which samples can be attached in a way that half of the sample is exposed and can be bent. The bending occurs at a fixed anvil with rounded edges next to the rotatable disk. The flex-e-test measurement setup is shown in Fig. 9 (a). Fig. 9 (b) shows in detail the bending surface and Fig. 9 (c) schematically demonstrates the bending of the film in tension. The bending radius is determined by the distance between the rotatable wheel and the anvil. During the experiment, this distance was adjusted to 2 mm, which corresponds to a strain of 1.25% in the film. Every sample underwent 10000 bending cycles.
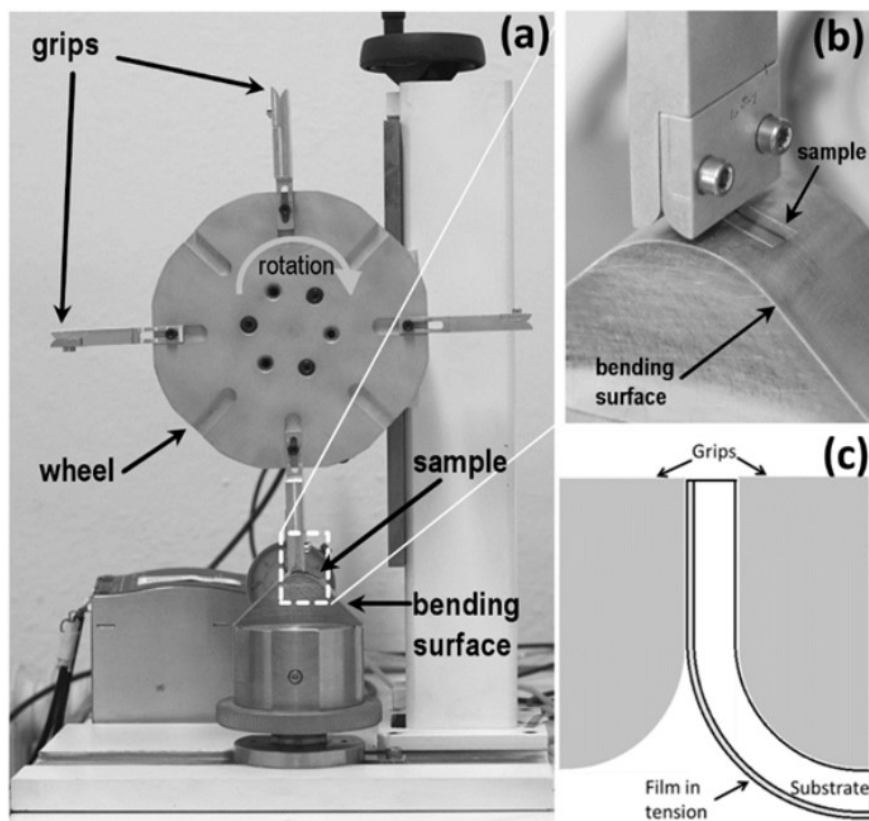
Fig. 9: Bending test setup consisting of a rotatable wheel with grips for sample fixation and a bending surface. The bending radius is determined by the distance between the anvil and the wheel [48]*.*

Post-mortem scanning electron microscopy

After tensile straining and bending tests, the surface of the samples was scanned using a Zeiss Leo 1525 SEM to investigate the damage. An acceleration voltage of 5 kV was applied, and the imaging occurred using either InLens or secondary electron detectors. Every sample was imaged at least at three different positions.

4. Results and discussion

In the following, the results obtained within this thesis will be presented and discussed. This chapter will start with the thickness and chemical composition of the films, followed by their structure, their electrical characteristics, and their mechanical properties as evaluated by tensile strain measurements, bending tests and post-mortem SEM.

4.1 Thickness and chemical composition

The thicknesses and planned chemical compositions of the synthesized AgAuSi TFMGs were calculated using the sputtering rates of the single targets and the deposition time. In order to verify both, SEM, EDX and XRR characterizations were performed. The thickness of the deposited films was measured using SEM for the 1000 nm and 500 nm thick films and XRR for 25 and 12 nm thick films, as described in the previous chapter. The deviation of the measured thickness from the desired thickness was below 10% in all cases.

The chemical compositions were reviewed with EDX measurements. Table 1 shows the planned compositions, the actual compositions and a designation for every synthesized AgAuSi TFMG. The stated designation will be used as a short name of the actual composition in this thesis. In addition to those samples listed in Table 1, binary AuSi and AgSi and a pure Au film were grown for comparison using similar deposition conditions. The EDX measurements revealed, that the actual Ag content is very close to the planned content. In contrast, the actual Au and Si contents show a larger deviation from the planned composition. The Au content is higher for all samples, and the Si content is accordingly lower.

To verify the uniformity of composition within the samples, multiple EDX scans were performed on selected samples. Within these measurements, composition differences of maximum 3% were detected. At the edges of the samples, higher Si contents were measured than in the centers of the samples. These fluctuations can be explained by the differences in the sputtering behavior of the single components. The atomic masses of Au, Ag and Si are 197 u, 108 u and 28 u respectively. During the sputtering process, the atoms, that were ejected from the target, collide with the Ar atoms in the vapor phase. The Ar atoms have a mass of 40 u. When a silicon atom collides with an Ar atom, it will be scattered more than an Ag or Au atom. This leads to a surplus of Si atoms at the outer dimensions of the sample, and accordingly higher Au and Ag concentration in the center of the samples. As Au is by far the heaviest of the sputtered atoms, the resulting lowest scattering of Au could be the reason for the measured high Au contents of the TFMGs.

Table 1: The planned compositions, the actual compositions as measured by EDX and the short designations of the deposited AgAuSi TFMGs.

Designation	Planned/actual chemical composition [at%]		
	Au	Ag	Si
$Ag_{70}AuSi$	10 / 12	70 / 70	20 / 18
$Ag_{60}AuSi$	20 / 24	60 / 60	20 / 16
$Ag_{50}AuSi$	30 / 34	50 / 50	20 / 16
$Ag_{40}AuSi$	40 / 45	40 / 39	20 / 16
$Ag_{30}AuSi$	50 / 56	30 / 29	20 / 15
$Ag_{20}AuSi$	60 / 65	20 / 20	20 / 15
$Ag_{10}AuSi$	70 / 74	10 / 12	20 / 14

4.2 Structural properties

To verify the amorphous structure of AgAuSi TFMGs, the samples have been characterized by XRD and TEM. Additionally, T_g and T_x, which are characteristic for every MG, were determined by DSC.

4.2.1 X-ray diffraction

Within this chapter, the X-ray diffractograms of AgAuSi TFMGs in the as-deposited state as well as in distinct time intervals after deposition will be presented and discussed. Then, the diffractograms of AuSi and AgSi TFMGs with different Si contents will be shown.

Fig. 10 shows the X-ray diffractograms of the AgAuSi TFMGs with different compositions in the as-deposited state obtained for 500 nm thin films. The intensity scale of the diffractograms of $Au_{80}Si$, $Ag_{10}AuSi$, $Ag_{70}AuSi$ and $Ag_{80}Si$ are scaled down by the factors indicated in the diagram. These scaled down diffractograms have peaks of high intensity, which evidence a crystalline or nanocrystalline nature of the films. For compositions with an Ag content of 20-60 at%, a broad peak of low intensity is observed. Additionally, a very broad and low intensity hump can be seen at a higher 2θ angles. These characteristics are typical for amorphous metals [8].
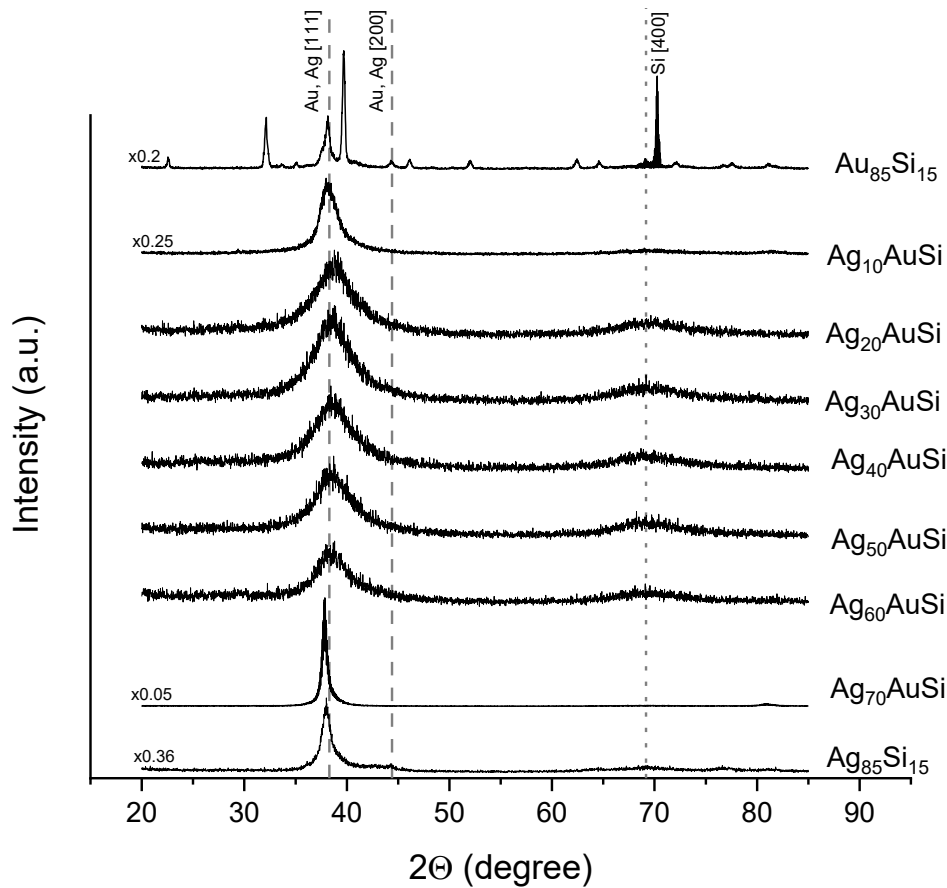
Fig. 10: X-ray diffractograms of 500 nm thick AgAuSi films of varying chemical compositions in the as-deposited state

.

To illuminate the stability of Au-based TFMGs at room temperature, the diffractograms were remeasured after the time intervals of 24 h, 1 week, 8 weeks and 8 months. In order to distinguish and quantify the changes in the measured patterns, the peaks were fitted with a Voigt function using a Levenberg-Marquardt algorithm in Origin. From the fitted peaks, the peaks positions and the full width at half maximum (FWHM) values were obtained.

The peak positions obtained for the different compositions of the 500 nm thin AgAuSi TFMGs in the as-deposited state and after time intervals of up to 8 months are displayed in Fig. 11 (a). Error bars are added for every data point, however, in some cases, they are smaller than the size of data point symbol. The errors were estimated in Origin according to the error propagation formula and scaled by the square root of the reduced Chi-square (Origin's standard error). The horizontal lines in the diagram indicate the positions of the Ag[111] and Au[111] peak for comparison [49][50].

Different trends for different compositions can be detained from the data presented in Fig. 11 (a). Films with an Ag content between 40 at% and 60 at% are characterized by peak positions at a 2θ angle of about 38.6° and show no peak shift over the observed interval of 8 months. The $Ag_{30}AuSi$ composition behaves very similar to the samples with Ag contents between 40% and 60%. However, the peak appears to slightly shift to lower angles after 8 months. In the sample with an Ag content of 20 at%, the as-deposited peak position is significantly higher than the peak positions of the other amorphous samples. Over the observed time interval, a significant peak shift was observed, where the final peak position was 0.45° smaller than the initial peak position, and also distinctly lower than the peak position of other amorphous samples. As can be seen in Fig. 11 (a), the samples with crystalline XRD patterns, i.e. $Ag_{10}AuSi$ and $Ag_{70}AuSi$, have a smaller 2θ angle than the amorphous samples. The $Ag_{10}AuSi$ sample exhibits a trend similar to the $Ag_{20}AuSi$ sample, where the peak shifts to lower angles after the deposition. The sample with a Ag content of 70 at% has the lowest 2θ angle, that seems to be constant for the observed time interval.

The FWHM for the different compositions and time intervals after deposition for 500 nm TFMGs is given in Fig. 11 (b). Again, error bars are displayed for every data point, but are too small to be seen for some points. The FWHM has a trend very similar to the peak positions, where the 500 nm thick samples with Ag contents between 30 at% and 60 at% have approximately the same FWHM, which is also constant in the observed time interval of 8 months. The sample with an Ag content of 20 at% shows the trend of decreasing FWHM over 8 months. The same trend occurs for an Ag content of 10 at%, however, there the FWHM is lower for the $Ag_{10}AuSi$ sample than for the $Ag_{20}AuSi$ sample for all observed time intervals. The sample with an Ag content of 70 at% has the lowest FWHM, which is, like in the amorphous samples, constant over the observed time period of 8 months.
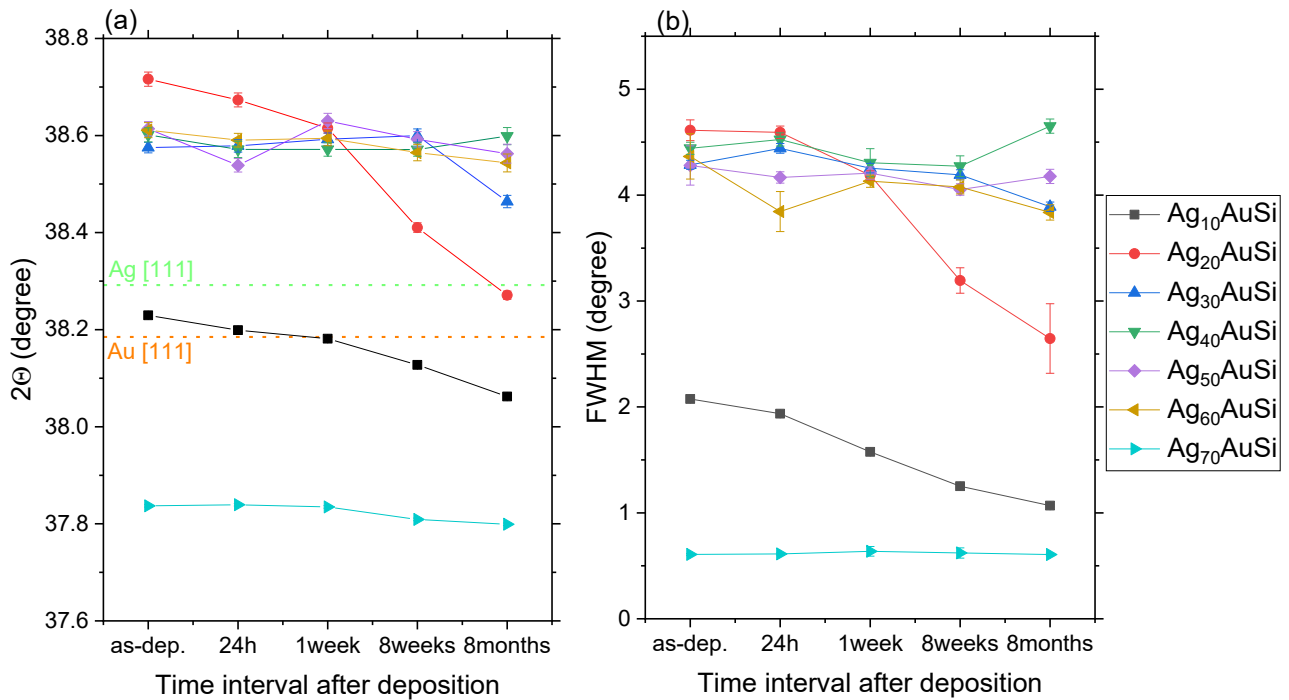
Fig. 11: (a) The peak positions of 500 nm thin AgAuSi TFMGs in as-deposited state (as-dep.) and after time intervals of 24 h, 1 week, 2 weeks and 8 months. Horizontal lines indicate the Ag[111] and Au[111] peaks taken from [49][50]. (b) FWHM of 500 nm thin AgAuSi TFMGs in as-deposited state (as-dep.) and after time intervals of 24 h, 1 week, 2 weeks and 8 months.

The X-ray diffractograms obtained for Ag compositions between 30 at% and 60 at% have broad peaks of low intensity, which are typical for metallic glasses [8]. In the literature [8], such patterns are often used to confirm the amorphous state of the samples. However, XRD measurements do now allow to unambiguously distinguish between small volume fractions of crystals and a fully amorphous structure. Therefore, it cannot be completely excluded, that nanocrystals are present in the AgAuSi TFMGs [7][8]. According to the XRD analysis presented in Fig. 11 (a), AgAuSi systems with Ag content between 30 at% and 60 at% are stable over the period of 8 months proving that the unstable AuSi system, which will be discussed with the following along with Fig. 12, can be stabilized by the substitution of sufficient amounts of Au by Ag. In the samples with an Ag content of 20 at%, the shift of the peak towards the Au [111] position and the declining FWHM as shown in Fig. 11 (a) and (b) indicate crystallization in the sample or growth of already crystalline regions within the amorphous matrix. The peak shift and decrease of FWHM in the $Ag_{10}AuSi$ sample can be attributed to lattice relaxations. In contrast to this, $Ag_{70}AuSi$ has a constant peak position and FWHM over the observed time. However, the peak position differs by 0.5° from the Ag [111] peak. This could be due to lattice strains as well.

In addition to the AgAuSi system, the AgSi as well as the AuSi system were studied. However, these systems were studied in less detail, because they are unstable, as shown in the literature for AuSi [34], and as investigated for AgSi within this thesis. In the AgSi system, delamination occurred shortly after the deposition. In both the AgSi and AuSi systems, crystallization at the surface seemed to occur, as inferred from a color change of the samples. The crystallization process of the unstable 500 nm $Au_{80}Si$ TFMGs is evident from the X-ray diffractograms in Fig. 12. In the as-deposited state, various peaks which stem neither from Au nor Si are measured. These peaks could indicate metastable crystalline Au_xSi phases, that were studied in detail in the literature [51]. After 8 months, these peaks vanish, with only the Au peaks remaining.
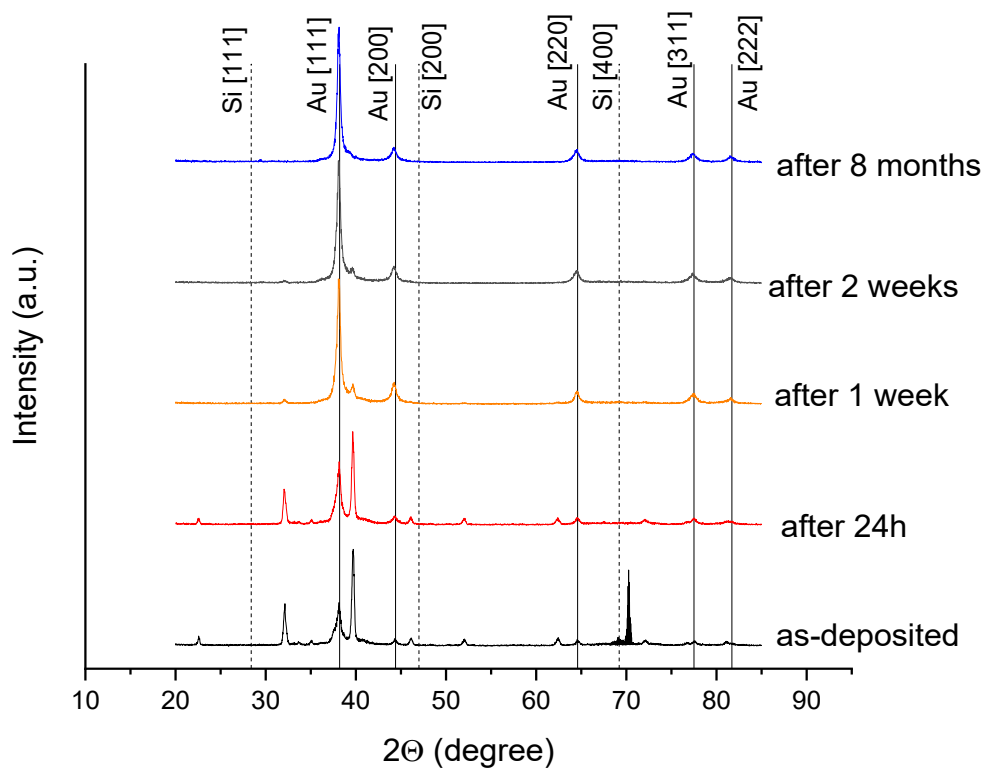
Fig. 12: X-ray diffractograms of 500 nm thin $Au_{80}Si$ TFMGs in as-deposited state and after time intervals of 24 h, 1 week, 2 weeks and 8 months.

For both the AuSi and the AgSi system, films with different compositions were deposited. Fig. 13 shows the diffractograms of three different AuSi (a) and five different AgSi (b) compositions, all of them in the as-deposited state. With increasing Si content, the numerous peaks present in $Au_{80}Si$ vanish to only two peaks in $Au_{70}Si$ and $Au_{60}Si$. These peaks have a significantly lower intensity and are broader, which indicates at least a partially amorphous structure of the films. The two obtained peaks suggest a coexistence of two

25

amorphous phases. To fully understand the atomistic structure of AuSi films of different compositions, TEM analysis is needed. Within the AgSi system, compositions with Si contents ranging from 10 at% to 50 at% were studied. Even for very high Si contents, the films seem to be crystalline, as evidenced by a sharp Ag [111] peak. With increasing Si content, this peak broadens and lessens in intensity. However, no Si peak is visible even for the sample with 50 at% Si content.

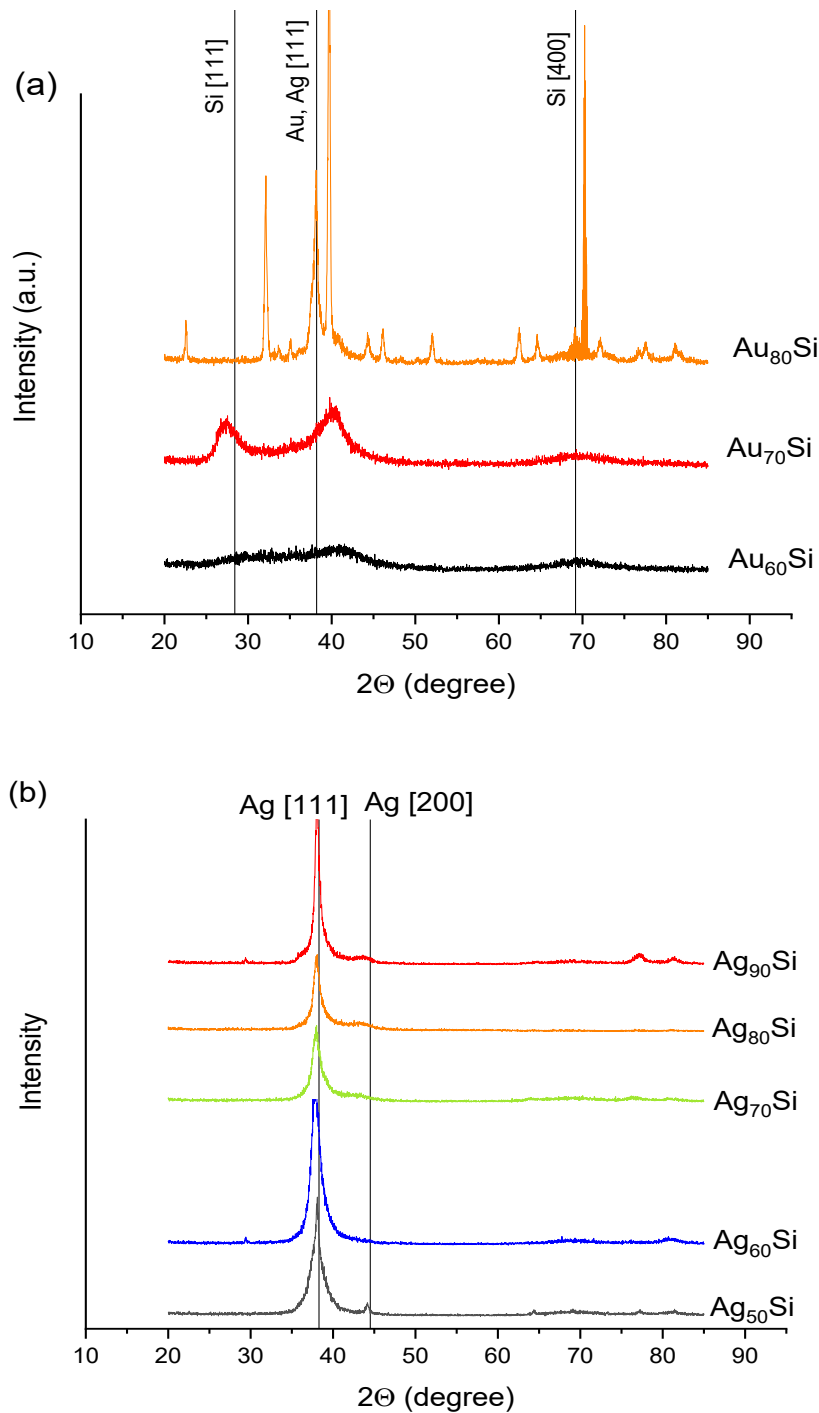*Fig. 13: X-ray diffractograms of films with different (a) AuSi and (b) AgSi compositions in the as-deposited state.*

26

4.2.2 Differential scanning calorimetry

For the investigation of T_g and T_x, DSC measurements were performed. In Fig. 14, the results are shown in an endothermic heat flow over temperature diagram. T_g can be seen as an increase in heat flow, as energy is consumed when the material is converted to a supercooled liquid [7][8]. As energy is released during crystallization, T_x appears as negative peak. Arrows mark the corresponding temperatures for each composition. All compositions except $Ag_{70}AuSi$ show a glass transition temperature, which means, that all of these samples have amorphous volume portions.
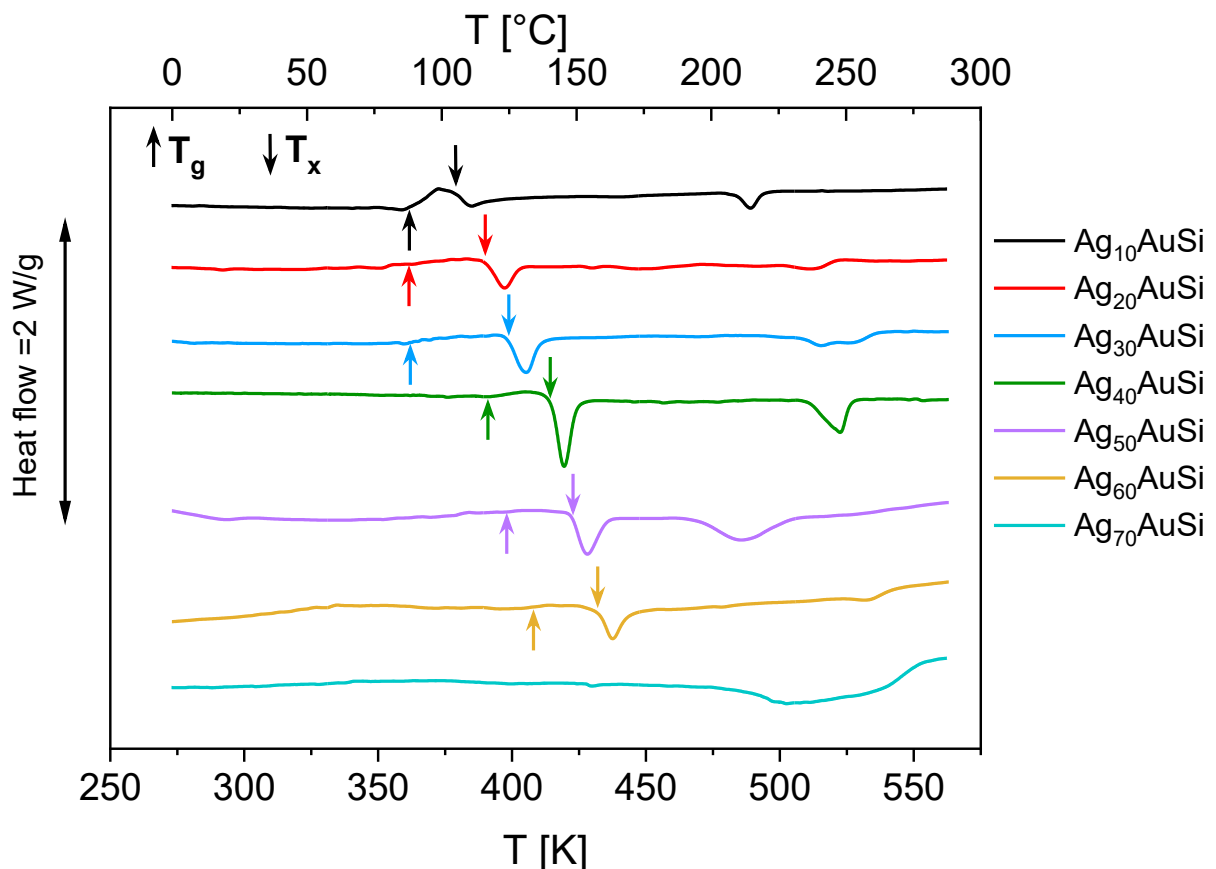
Fig 14: Endothermic heat flow diagram showing T_g and T_x for AgAuSi TFMGs. All compositions except $Ag_{70}AuSi$ exhibit a glass transition temperature. Up-pointing arrows indicate T_g, down-pointing arrows T_x.

To analyze the change in T_g and T_x with composition in more detail, T_g and T_x were plotted as function of the Ag content in Fig. 15 (a). In Fig. 15 (b), the supercooled liquid region ΔT_x is shown, which is the temperature difference between T_g and T_x [8]. T_x increases with increasing Ag content for all compositions. T_g appears to be constant with temperature for Ag contents between 10 at% and 30 at%, and then increases with increasing Ag content. The constant T_g and increasing T_x lead to larger stabilized ΔT_x regions with increasing Ag contents between 10 at% and 30 at%. Also, the exothermic crystallization peak increases with

increasing Ag content until the $Ag_{40}AuSi$ composition, from where on it decreases again. This is another indicator for the increasing crystallinity of the samples with high Ag or high Au contents.

Fig. 15: (a) T_g and T_x as function of composition. The T_x values appear to increase nearly linearly with Ag content, and the T_g values stay constant for Ag contents between 10 and 30 at% and then increase with Ag content as well. (b) ΔT_x increases for Ag contents between 10 and 30 at% and is constant for Ag contents between 40 and 60 at%.
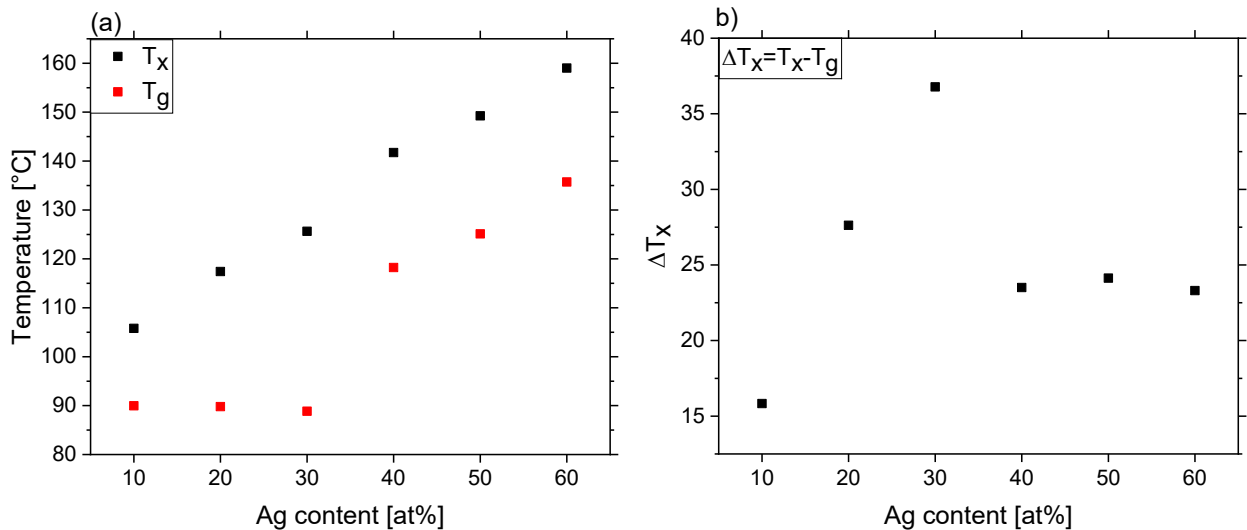
The results of the DSC measurements are in good agreement with the literature, where melt-spun $Au_xSi_{17}Cu_{75.5-x}Ag_{7.5}$ MGs had a T_g in the range of 100°C [36]. In $Au_xSi_{17}Cu_{75.5-x}Ag_{7.5}$ MGs, the sample with the highest Au content exhibited the lowest T_g, which appeared to be rather constant for an Au content for 75.5 and 70 at%, while T_x was increasing steadily with decreasing Au content. This led to an enlarged ΔT_x region at 65 at% Ag. In comparison with other MGs, that often exhibit a T_g above 300°C, Au-based MGs have a low T_g [52].

4.2.3 Transmission electron microscopy

As already mentioned, XRD cannot detect small volume percentages of nanocrystals in amorphous matrixes. Therefore, TEM measurements were performed on 25 nm thick TFMG samples deposited directly onto TEM grids. Fig. 16 a-g show the SAD patterns of AgAuSi TFMGs as well as HRTEM micrographs. In the samples with an Ag content of 10 at% in Fig. 16 (a) and 70 at% in Fig. 16 (g), the SAD clearly shows crystalline rings. This is in good agreement with X-ray diffractograms presented in Fig. 10, where a crystalline pattern was recorded. The $Ag_{20}AuSi$ sample in Fig. 16 (b) also exhibits crystalline rings. They are slightly less pronounced than in $Ag_{10}AuSi$, but still clearly visible. In the samples with Ag contents

between 30 at% and 60 at% in Fig. 16 (c-f), the crystalline rings merge to amorphous halos. Of these four compositions, $Ag_{40}AuSi$ and $Ag_{50}AuSi$ are very similar with no indications of crystallinity, and $Ag_{30}AuSi$ and $Ag_{60}AuSi$ mark the transition between amorphous and crystalline structure. The HRTEM micrographs reveal that some crystalline areas can be found in every composition. $Ag_{10}AuSi$ and $Ag_{70}AuSi$ TFMGs have the highest density of crystals, followed by $Ag_{20}AuSi$ and $Ag_{30}AuSi$ TFMGs. The samples with Ag content between 30 at% and 50 at% presented in Fig. 16 (c-e) exhibit only amorphous halos in the SAD patterns, however sparsely distributed very small (2 - 5 nm in size) crystallites can be observed in $Ag_{30}AuSi$ (Fig. 16 (c)) and $Ag_{50}AuSi$ (Fig. 16 (e)) compositions in the corresponding HRTEM images, as depicted by dashed white contours. Due to the small size and small volume fraction occupied by these crystallites, their contribution to the diffraction patterns is too weak to be distinguished from the contribution of the amorphous matrix. $Ag_{40}AuSi$ (Fig. 16 (d)) seems to be virtually fully amorphous although the existence of small crystallites cannot be completely excluded. The integrated intensities of the diffraction rings for all investigated samples are given in Fig. 16 (h) with the colors corresponding to the color of the frames in Fig. 16 (a-g). The compositions with Ag content of 10, 20 and 70 at% exhibit multiple peaks indicating medium and long-range order. The $Ag_{60}AuSi$ sample demonstrates rather weak peaks at the reciprocal vector values of 6.7 nm^{-1} and 7.8 nm^{-1}. As for the compositions with Ag contents between 30 at% and 50 at%, rather marginal differences can be detected indicating that the diffraction pattern is predominantly defined by the amorphous phase. The obtained results clearly demonstrate, that both XRD and DSC are not able to detect small crystals in an amorphous matrix. Even TEM SAD patterns are barely sensitive enough to distinguish between fully amorphous state and amorphous matrix with sparse nanocrystals. However, the HRTEM images could be used to identify the presence of small crystallites in an amorphous material.
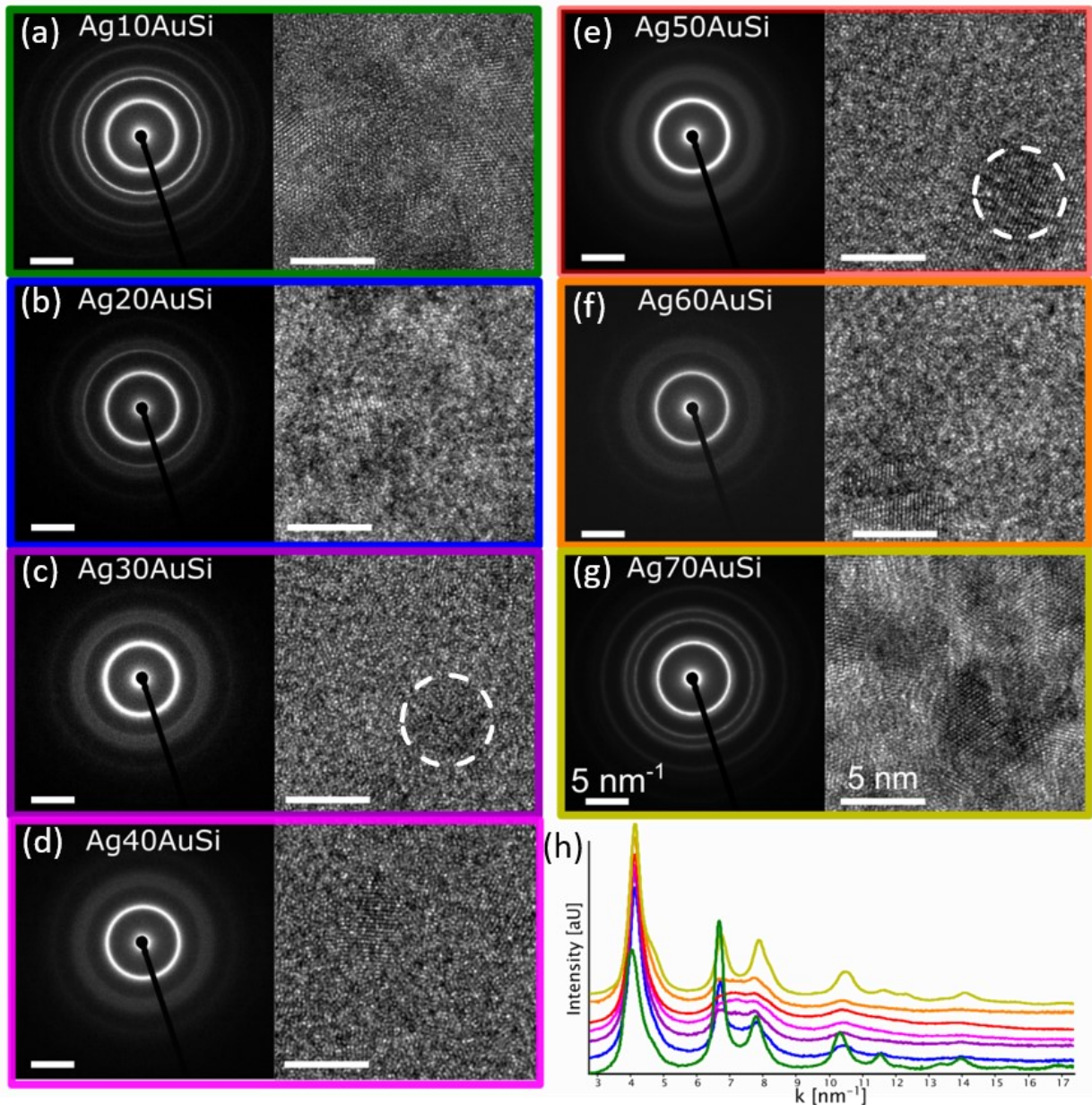
Fig. 16 (a)-(g): SAD and HRTEM micrographs of AgAuSi TFMGs. Ag₁₀AuSi (a) and Ag₇₀AuSi (g) TFMGs have crystalline rings in the SAD and a high crystal density. In (c) and (e), dashed white contours mark crystalline areas as detected by a darker contrast. Samples with a more equal Ag and Au content are characterized by amorphous halos in the SAD and only small crystalline areas embedded in an amorphous matrix. The SAD patterns were taken from areas of 150 nm in diameter. (h) Integrated intensities of the diffraction rings for AgAuSi TFMGs.

4.3 Electrical properties

The resistivities of the samples were measured with the van der Pauw method and with 4-point resistivity tests. The resistivity of a material strongly depends on its structure [53]. Therefore, resistivity measurements do not only indicate the material's suitability in electrical applications, but also complement the performed structure measurement methods.

Fig. 17 shows the resistivity measured in the van der Pauw geometry for the different material compositions and thicknesses. The resistivity values of 500 nm and 1000 nm thick $Ag_{40}AuSi$ and $Ag_{50}AuSi$ TFMGs are in good agreement with resistivity values of other Au-based MG reported in the literature [36]. For different thicknesses and compositions, two trends can be derived. Firstly, the resistivity decreases for high Ag or high Au values, respectively. This can be easily explained in combination with the findings derived by XRD (as seen in Fig. 10) and TEM (as seen in Fig. 16), where the samples with high Ag or high Au contents are crystalline. In contrast to this, high resistivity values were measured in samples with low crystallinity. The composition with an Ag content of 50 at% has the highest resistivity for all thicknesses. As the resistivity increases with atomic disorder (amorphous structure) [53], this result is a bit surprising since according to the TEM analysis (Fig. 16) the $Ag_{40}AuSi$ composition should have the lowest crystallinity. However, the resistivity is not simply proportional to the crystallinity and generally the resistivity values of complex disordered alloys are still not well understood [54].

The second trend is that thinner films have lower resistivities, which is in contrast to an increasing resistivity of thinner films based on crystalline metals [2]. For films with a thickness of 12 nm and 25 nm, approximately the same resistivity was measured, whereas the 50 nm thin films have a higher resistivity. The 500 nm and 1000 nm thin films again are characterized by very similar resistivities, which are about 40 µΩcm higher than the resistivities of the thinnest films. However, the composition with an Ag content of 70 at% does not follow this trend, and has similar resistivities for all thicknesses. The observed decrease of the resistivity with the film thickness is a very unexpected effect, which currently cannot be clearly explained, but which could be linked to a different degree of crystallinity in films with different thicknesses. As a potential explanation of this effect one should note the different deposition times used for the different film thicknesses. As mentioned in chapter 3, *Methods*, the deposition time varied between 14 s and 20 min for the AgAuSi TFMGs deposited in this thesis. With increasing deposition time, the targets as well as the substrate are heated by the impact of ions and sputtered atoms [40]. The influence of the temperature rise in the target can be neglected, as the targets are cooled and reach a temperature equilibrium within seconds [55], and the shutters are opened after this equilibrium was

reached. In contrast to that, an increasing temperature of the substrate over the course of a minute was described by Jörg et al. [56]. The higher substrate temperature could possibly cause an effect called amorphous annealing during the deposition process. In the literature, sputter deposited TFMGs with a certain degree of crystallinity in the as-deposited state were reported [57]. By annealing these samples in the ΔT_x regime between T_g and T_x, the crystals were dissolved into the amorphous matrix. AgAuSi TFMGs have a low glass transition temperature between 90°C and 140°C (Fig. 15). Even though the temperature as recorded with a sensor behind the substrate holder was measured to be below 35°C, the temporary local temperature at the film surface could be well beyond that, possibly reaching the ΔT_x regime. Small crystalline areas within the TFMGs could thus have been dissolved into the amorphous matrix. Another explanation was suggested by Magagnosc et al. for PdCuSi TFMGs deposited at different temperatures ranging from 25°C to 280°C [58]. Their results suggest a higher crystallinity for lower substrate temperatures, which were explained by the adatom mobility but also by a higher oxygen content in the low-temperature sample. As a high oxygen content was measured in the sample grown at the lowest substrate temperature (i.e. room temperature) and the second highest substrate temperature (i.e. at 210°C), and only the room temperature deposited sample was found to be crystalline, the influence of the oxygen content was concluded to be insignificant to the structural trend. Also, both oxygen contamination and low substrate temperatures inhibit the migration of atoms to their ideal (crystalline) lattice sites according to thermodynamical equilibrium [44][59]. Therefore, the obtained crystalline structure of the sample with the lowest adatom mobility and the highest oxygen content seems counterintuitive. In order to understand the reason for different resistivities (and therefore crystallinities) in AgAuSi TFMGs of different thicknesses, TEM investigations of the AgAuSi TFMGs cross sections for different film thicknesses are necessary.
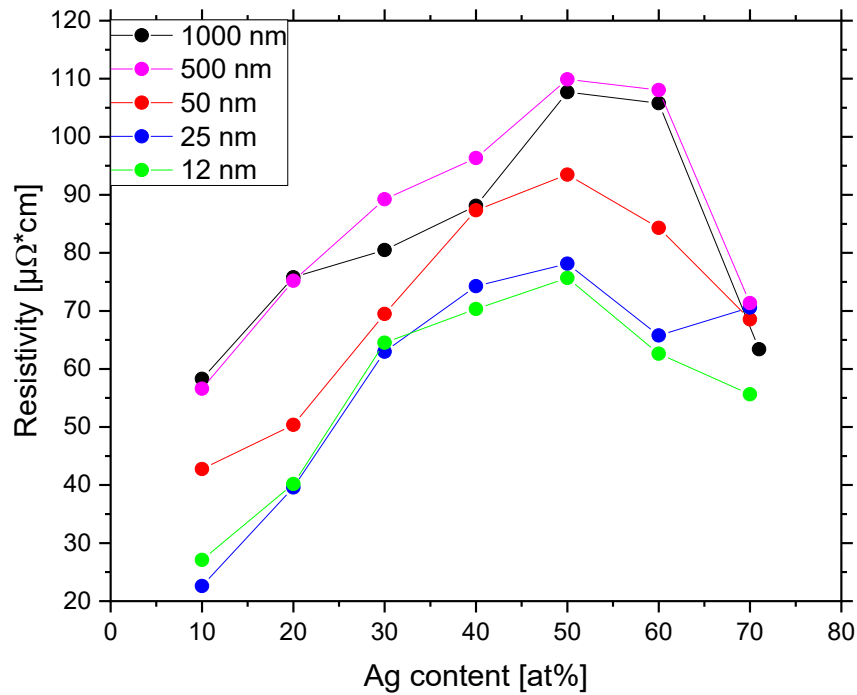
Fig 17: Resistivity measured with van der Pauw method for AgAuSi TFMGs with different compositions and thicknesses.

In addition to the van der Pauw method, the resistivity was also measured by a 4-point-probe as used in microelectronics. The resistivities obtained by these two methods are compared in Fig. 18 for two different film thicknesses, i.e. 50 nm and 500 nm. For both measurement methods, the 50 nm thin film has a lower resistivity than the 500 nm thin film. The 4-point resistivity values are higher for all compositions except for $Ag_{70}AuSi$. A different trend can be observed for the two different measurement methods. In van der Pauw resistivity measurements, the $Ag_{50}AuSi$ has the highest resistivity. In 4-point resistivity measurements, the highest resistivity was obtained for $Ag_{20}AuSi$, which is in contrast to the relatively low resistivity of this composition determined by the van der Pauw method. As TEM scans proved a high density of crystals in $Ag_{20}AuSi$, the van der Pauw methods appears to be the more accurate. Inaccuracies in the 4-point resistivity measurement could stem from finite sample sizes, thin sample thicknesses or contact errors, where the measurement tips could possibly penetrate the relatively soft Au-based TFMGs [60].
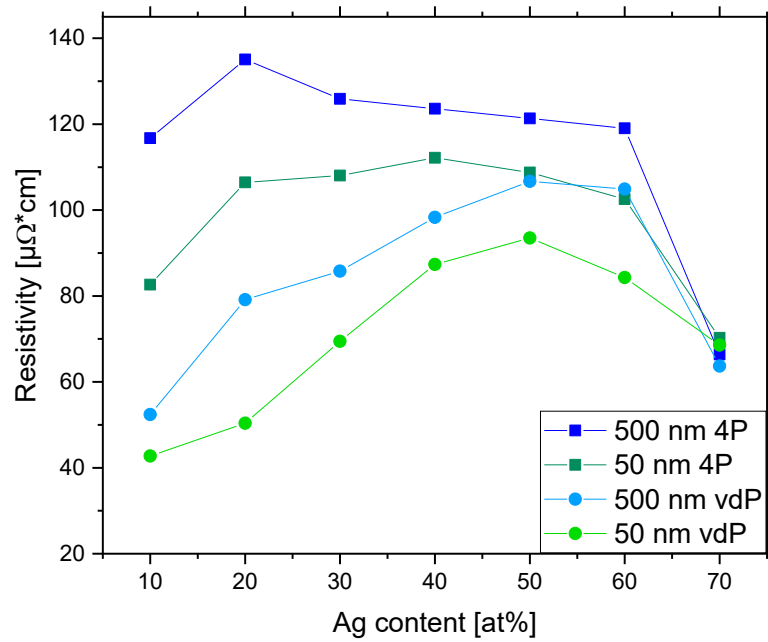
Fig 18: Resistivities measured with 4-point resistivity tests (4P) and van der Pauw method (vdP) for 50 nm and 500 nm AgAuSi TFMGs with different compositions and thicknesses.

4.4 Mechanical properties

4.4.1 Tensile tests

In order to estimate the suitability of AgAuSi TFMGs as flexible electrodes, the electrical resistance under tensile strain was measured. During straining, the resistance of the samples increases due to two mechanisms [61]. The first one is the geometrical change of the sample. As it becomes thinner and longer, the resistance increases constantly. Assuming a constant volume of the sample, the relative resistance change due to the geometry is identical for every material, and is called the constant volume approximation. The second mechanism that increases the resistance of a strained sample is the material damage. In TFMGs, typically long cracks appear, which drastically increase the resistance of the sample [27]. To estimate the strain, at which the first cracks are formed, the resistance increase measured during straining can be compared to the constant volume approximation [61]. The crack onset strain (COS) was defined as the strain, where the resistance of the strained sample deviated 5% from the constant volume approximation.

Fig. 19 shows the resistance divided by the starting resistance as function of the applied strain for different composition and thicknesses. The COS for the different thicknesses and compositions is displayed in Fig. 20. Additionally, the typical elastic limit for MGs of 2% is marked [10]. Except for the 500 nm and 1000 nm thick $Ag_{70}AuSi$ films, which are crystalline, all measured COS values lie distinctly above this limit, proving the exceptional behavior of AgAuSi TFMGs on polymer substrates. Due to size effects in MGs, the COS changes differently with thickness for every composition. In general, thinner films can sustain higher strains without failure as can be seen by the less drastic resistance increase of thinner films compared to thicker films in Fig. 19 and by the higher COS of thinner films in Fig. 20. As explained in chapter 2.1.1 *Mechanical properties*, this size effect can be explained by the suppression of shear bands in thinner films. Shear bands need sample sizes of 10 - 20 nm to fully develop and freely propagate [28]. When the sample dimensions are smaller than that, shear bands cannot form, and higher strains are endured without any plastic deformation or failure. Also, different trends with composition can be observed for different film thicknesses, that will be explained in detail.

The 1000 nm and 500 nm thin films exhibit similar behavior except for Ag contents of 10 at% and 20 at%. For both thicknesses, the samples with a higher crystallinity have a lower COS than the highly amorphous samples. This can be linked to extended plastic deformation in amorphous AgAuSi TFMGs. During straining of the material composite system, shear bands are formed in the amorphous layer, but no material separation takes place due to the support of the polymer. Therefore, the resistance is not increasing with the formation of a

shear band. This plasticity caused by the formation of shear bands was confirmed by straining 500 nm thin films up to 3%. They followed the constant volume approximation, which means, that no cracks were formed in the sample. In post-mortem SEM micrographs, that will be presented in chapter 4.2.2 *Post-mortem SEM analysis*, deformation marks were visible in the films after straining.

The 25 nm thin films have a trend opposite to the 1000 nm thin films. Here, the samples with higher crystallinity have a higher COS than the more amorphous samples with approximately equal Ag and Au contents. In the 12 nm films, the COS is significantly higher than the COS obtained for the other thicknesses for all compositions. For the sample with an Ag content of 20 at%, the COS is not reached until the applied strain or 10%, and for the samples where the COS was reached, only a minor resistance increase was measured. The COS of the 12 nm films scatters more than the COS of other thicknesses. This could be due to surface imperfections of the substrate, that induce damages to the film. As the films get thinner, the influence from the substrate becomes more prominent.
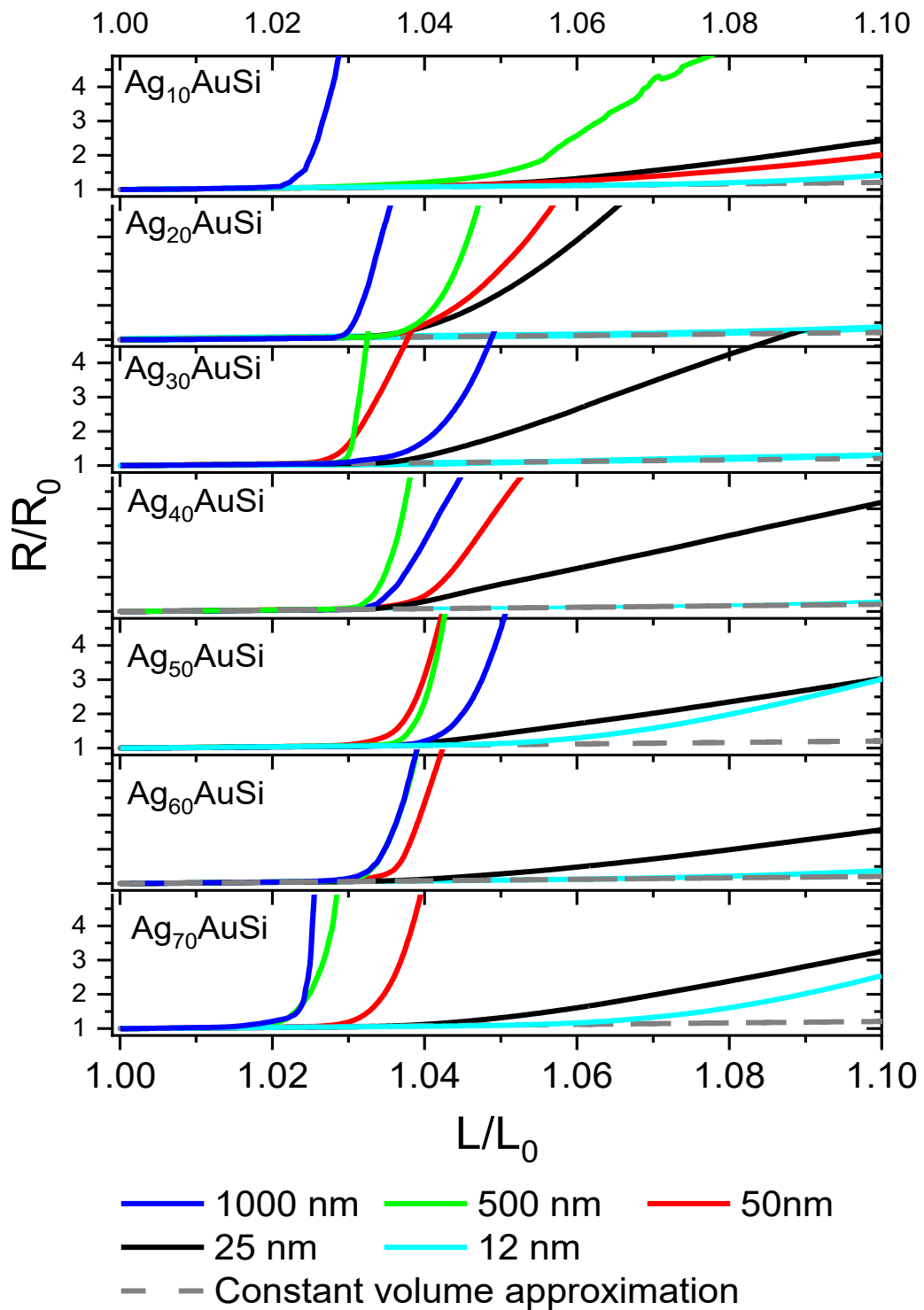
Fig. 19: Resistance as a function of tensile strain for AgAuSi TFMGs with thicknesses between 12 nm and 1000 nm. Thinner films can sustain higher strains without dramatic resistance increase.
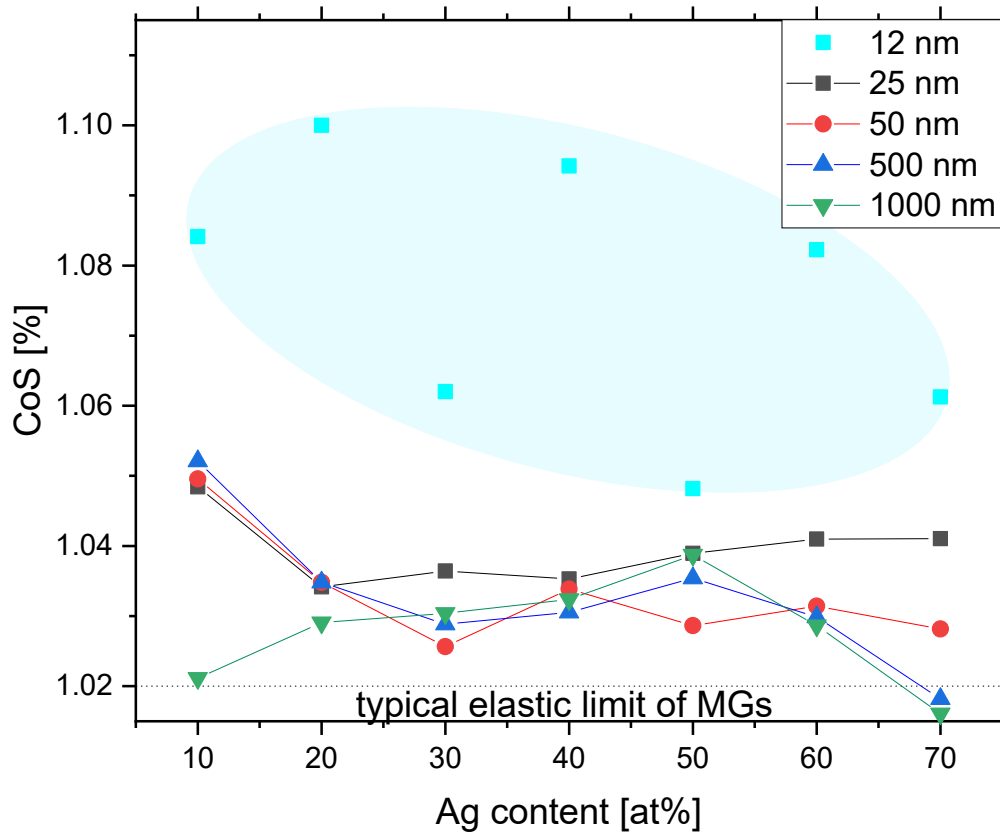
Fig. 20: Crack onset strain (COS) of AgAuSi TFMGs with film thicknesses between 12 nm and 1000 nm, and the typical elastic limit of MGs as reported in the literature [10]*.*

4.4.2 Post-mortem SEM analysis

After straining the samples, they were characterized by post-mortem SEM investigations. Detailed micrographs for all compositions and film thicknesses between 25 nm and 1000 nm are presented together in Fig. 21. The 12 nm thin films were not added, as they did not exhibit any cracks. The crack morphology is changing with thickness and composition of the samples. The samples with Ag contents between 20 at% and 60 at% behave comparable to other TFMGs on polymer substrates reported in the literature [27]; The 500 nm and 1000 nm thin films have long cracks perpendicular to the straining direction. The crack edges are not perpendicular to the film surface but have steps. This indicates that the cracks formed due to the subsequent activation of multiple shear bands during the local fracture process. These samples also exhibit shear bands, which can be seen in Fig. 21 as very fine lines in angles between 45° and 50° with respect to the straining direction. The red arrow in the Ag$_{50}$AuSi 500 nm micrograph points at one of these shear bands. The thinner films have a different

crack morphology. The cracks are still perpendicular to the straining direction, but are thinner and not as straight as the cracks in the thicker samples. The 25 nm thin films have even finer and wavier cracks than the 50 nm thin films, and are even shorter. These results are in very good agreement with previous work on TFMGs, where size effects and shear band suppression were detected for ultrathin films [27].

The partially crystalline samples behave differently. In $Ag_{70}AuSi$, the cracks in the 500 nm and 1000 nm thick samples have clearly crystalline features, where cracks are not only perpendicular to the straining direction and are opened wide. The 25 nm and 50 nm thin films look similar to the other compositions with short, wavy cracks. The sample with an Ag content of 10 at% already stood out due to high COS values, which are well explained by the SEM micrographs. The 500 nm thin sample has a crack morphology similar to the amorphous samples. However, fewer cracks were observed for this composition, and most of the cracks appeared to stem from inhomogeneities of the polymer substrate, that functioned as crack nucleation site. The 1000 nm thin sample exhibits a completely different behavior. In this film, only small cracks of a few nm were found, but no larger cracks as in amorphous samples. Also, these samples curled up after straining, indicating a plastic deformation of the film, which was not observed for other compositions or thicknesses. In the 25 nm and 50 nm thin samples, only extremely small cracks could be detected, that again nucleated at inhomogeneities from the polymer substrate, where the local stress exceeds the applied stress significantly.
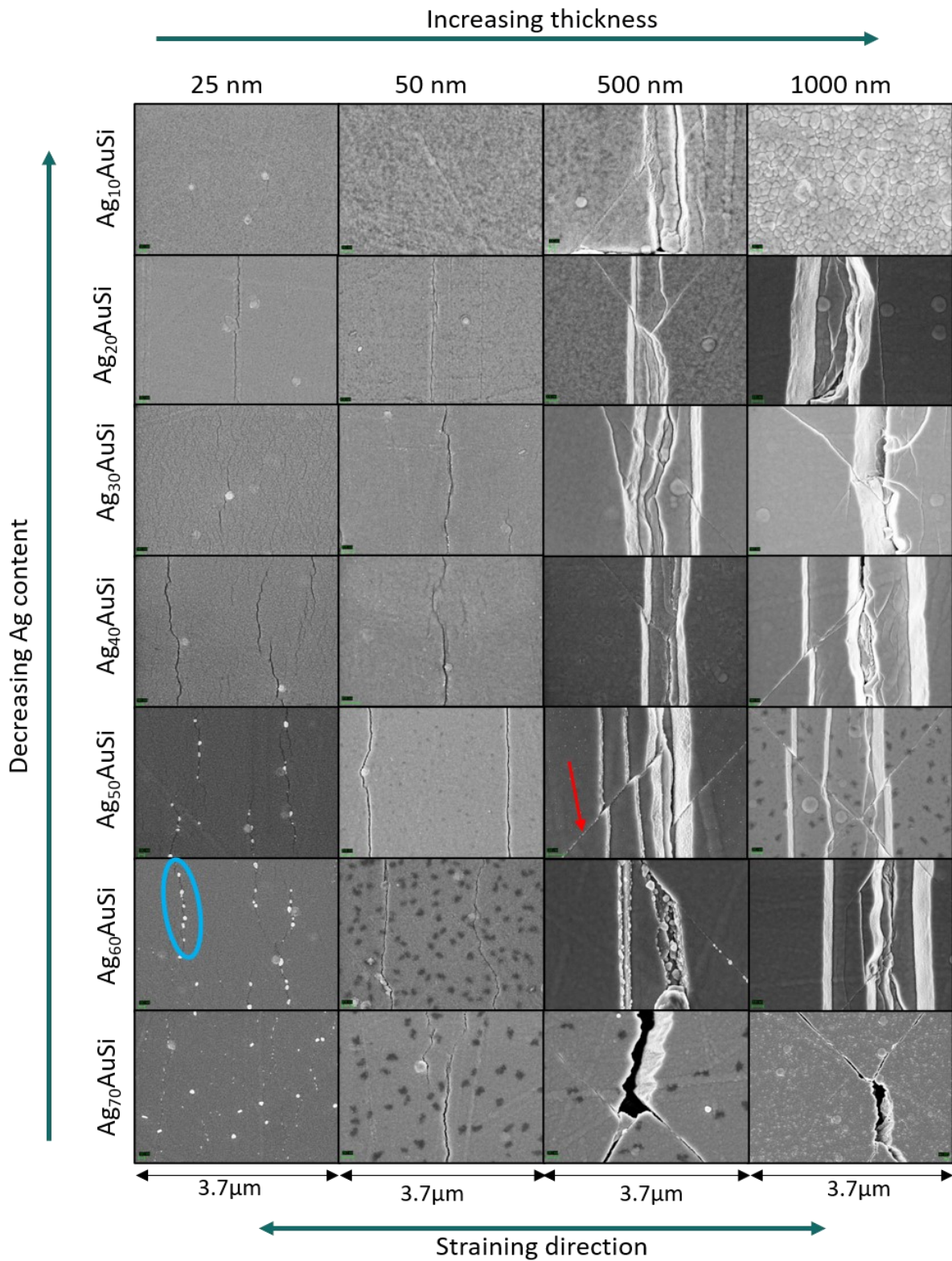
Fig. 21: Post-mortem SEM micrographs of AgAuSi TFMGs with the different compositions and film thicknesses after straining to 10 %. In the horizontal direction, the different thicknesses of the respective compositions are shown, with increasing thicknesses from left to right. In the vertical direction, the different compositions are listed, with increasing Ag content from top to bottom. The blue ellipse exemplarily frames Ag agglomerations, and the red arrow points at a shear band.

Another notable feature are the white dots that appear on top of cracks and shear bands in Ag rich samples for all thicknesses. The blue ellipse in the micrograph of the 25 nm $Ag_{60}AuSi$ TFMG exemplarily frames this surface feature. These dots are believed to be Ag agglomerations which diffused on the surface during the local fracture events. Ag is known to be highly diffusive and can form surface precipitations in thin films after deposition even without applied mechanical strain [62]. The dark spots that appear on some surfaces (e.g. $Ag_{60}AuSi$, 50 nm) are visible only using the in-lens SEM detector and are not detectable in secondary electron images, therefore they are believed to be surface contaminations.

As already mentioned in chapter 4.2.1 mechanical properties, plastic deformation of TFMGs was demonstrated by straining AgAuSi TFMGs up to 3% followed by SEM measurements. During straining, the resistivity of the samples followed the constant volume approximation, which means, that no cracks were formed. Fig. 22 is an SEM micrograph of a 500 nm thin $Ag_{50}AuSi$ film in two different magnifications after 3% straining, which is representative for all TFMG compositions investigated in this thesis. As marked in the micrograph, the strain was applied in horizontal direction. The white lines perpendicular to the straining direction are deformation steps resulting from the formation of shear bands in the film. As MGs are known for their brittle-like behavior, where shear bands lead to catastrophic failure [7], this micrograph evidences the superior properties of TFMGs on polymer substrates, where plastic deformation by shear bands occurs without failure due to the support of the polymer.
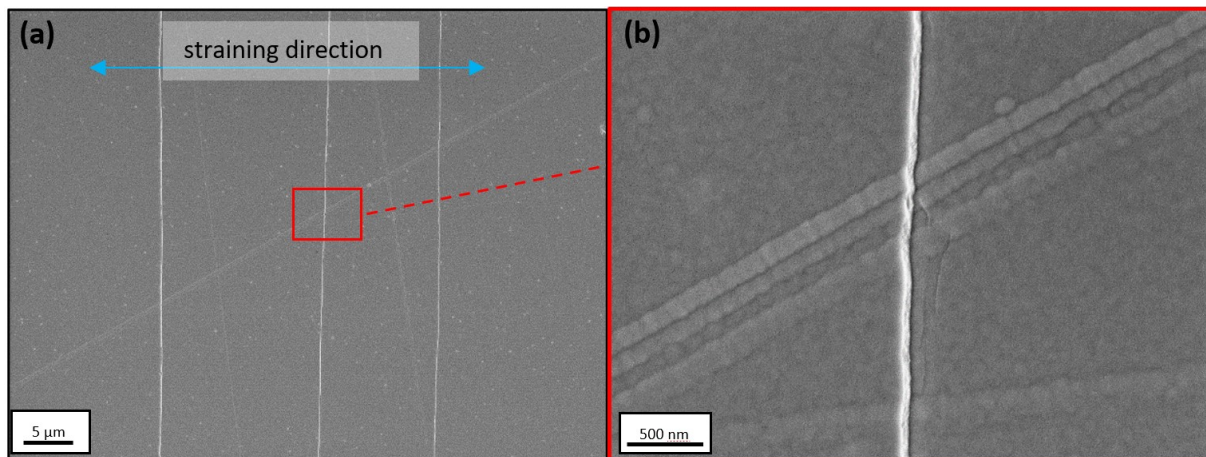

Fig. 22: Post-mortem SEM micrographs showing deformation steps on 500 nm thin $Ag_{50}AuSi$ TFMG after 3% straining. Micrograph (b) is a zoom of micrograph (a) at the position marked with a red rectangle.

SEM scans were also used to evaluate the material damage after cyclic bending test. The applied bending strain was 1.25%, which is below the elastic limit for a MG, but above the elastic limit for a crystalline metal [10]. The bending strain corresponds to a bending radius of 2 mm, which is realistic for real applications. Fig. 23 shows SEM micrographs of a 1 µm thick $Ag_{20}AuSi$ TFMG (a) and a 1 µm thick Au film on polymer substrate (b) after 10000 bending cycles. Due to the dissimilar sizes of the surface features of the samples, micrographs of different magnifications are presented. No damage was found in the TFMG shown in the SEM micrograph nor in any other TFMG. Even near surface defects as in Fig. 23 (a), where strain localization occurs, no cracks were observed. Contrary to this, the crystalline Au film exhibits multiple cracks and severe surface roughening. This simple test demonstrates the superior performance of TFMGs in flexible electronics compared to conventional crystalline films.

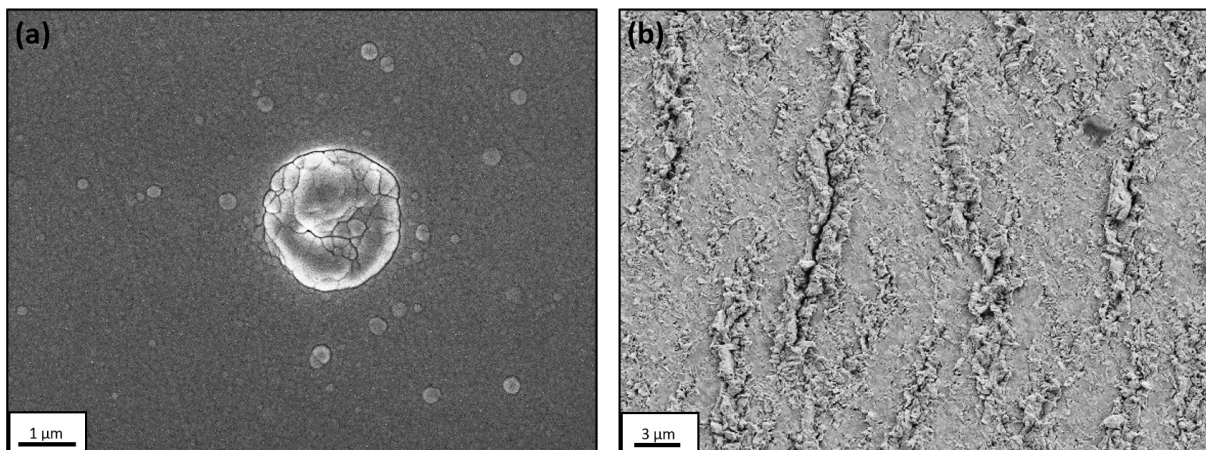*Fig. 23: SEM micrographs of a 1 µm thick (a) $Ag_{20}AuSi$ and (b) Au film after 10000 cycles of bending with a bending radius of 2 mm. In (a), no cracks were observed even at high magnifications near surface defects, whereas in (b) typical fatigue damage was found.*

42

5. Conclusions and Outlook

In this work, novel $Ag_xAu_{85-x}Si_{15}$ thin film metallic glasses (TFMGs) were fabricated and systematically investigated for their structural, electrical and mechanical properties. The aims of this thesis were to characterize the influence of the composition and thickness on the properties of this TFMG system and to find material combinations with high potential for future applications like flexible electronics.

X-ray diffraction yielded broad, low intensity peaks, that are typical for metallic glasses, for compositions with Ag contents between 20 at% and 60 at%. Differential scanning calorimetry confirmed these results, as for all compositions except for $Ag_{70}AuSi$ glass transition was detected. However, transmission electron microscopy revealed significant amounts of crystalline areas for Ag contents of 20 at% and 60 at% and very small (2-5 nm) crystallites sparsely distributed in an amorphous matrix for Ag contents of 30 at%, 40 at% and 50 at%. Despite the common approach of using X-ray diffraction and differential scanning calorimetry to confirm the amorphous state of metallic glasses, this thesis clearly shows that a certain degree of crystallinity cannot be excluded by these measurement methods.

The samples with high Au or high Ag content, respectively, had lower resistivities than samples with approximately equal Au and Ag content. This is in good agreement with the structural measurements, where the samples with high Au or Ag content had a higher degree of crystallinity. The resistivities for thinner samples were distinctly lower than the resistivities for thicker samples. In contrast to crystalline films, where the resistivity increases with decreasing film thicknesses, the resistivity of AgAuSi TFMGs was found to decrease with film thicknesses, leading to a resistivity of ultrathin (12 nm) $Ag_{20}AuSi$ TFMGs comparable to crystalline Au films with the same thickness. The different resistivities of films with different thicknesses could possibly be a result of the different kinetics of short and long depositions. For clarification, cross sectional TEM scans of thinner and thicker AgAuSi TFMGs would be necessary.

Tensile tests with in-situ resistance measurements revealed superior mechanical properties of AgAuSi TFMGs with a crack onset strain of 3% or more for most compositions and thicknesses, compared to a typical elastic straining limit of 2% for MGs and 0.5% for crystalline metals. Ultrathin (12 nm) AgAuSi stood out as values of 6-10% were measured. SEM measurements on AgAuSi TFMGs after straining suggested the suppression of shear bands as cause for the superior mechanical properties of thinner films. In bending tests, AgAuSi TFMGs demonstrated exceptional behavior, where no material damage occurred in cyclic bending tests after 10000 cycles with a bending radius of 2 mm, as compared to

crystalline Au films of the same thickness, where cracks were observed in post-mortem SEM micrographs.

The unique combination of electrical and mechanical properties makes AgAuSi TFGMs promising candidates for future application in flexible electronics. Additionally, the high noble metal content and the antimicrobial properties of Ag are promising for biomedical applications. In order to integrate AgAuSi TFMGs in future electronic devices, further research exceeding this thesis is underway, especially regarding the influence of the film thickness on the structure of the thin films as well as the electrical properties under high currents and high temperatures.

Literature

[1]		Sun, Yao, Warren, Barmak, Toney, Peale, and Coffey, "Surface and grain-boundary scattering in nanometric Cu films," *Phys. Rev. B - Condens. Matter Mater. Phys.*, vol. 81, no. 15, pp. 1–12, 2010, doi: 10.1103/PhysRevB.81.155454.

[2]		Gilani and Rabchuk, "Electrical Resistivity of Gold Thin Film," *Can. J. Phys.*, vol. 96, no. 3, pp. 272–274, 2018, doi: 10.1139/cjp-2017-0484.

[3]		Yiu, Diyatmika, Bönninghoff, Lu, Lai, and Chu, "Thin film metallic glasses: Properties, applications and future," *J. Appl. Phys.*, vol. 127, no. 3, 2020, doi: 10.1063/1.5122884.

[4]		Chen, Hsu, Chan, Duh, Lee, Jang, and Chen, "Antimicrobial properties of Zr-Cu-Al-Ag thin film metallic glass," *Thin Solid Films*, vol. 561, pp. 98–101, 2014, doi: 10.1016/j.tsf.2013.08.028.

[5]		Wang, Li, Li, Xiao, Chen, and Zhang, "Design and preparation of nanoporous Ag-Cu alloys by dealloying Mg-(Ag,Cu)-Y metallic glasses for antibacterial applications," *J. Mater. Chem. B*, vol. 7, no. 26, pp. 4169–4176, 2019, doi: 10.1039/c9tb00148d.

[6]		Chu, Huang, Jang, Wang, and Liaw, "Thin film metallic glasses: Preparations, properties, and applications," *Jom*, vol. 62, no. 4, pp. 19–24, 2010, doi: 10.1007/s11837-010-0053-3.

[7]		Suryanarayana and Inoue, *Bulk Metallic Glasses*, 2nd ed. Boca Raton: Taylor & Francis Group, 2018.

[8]		Miller and Liaw, *Bulk Metallic Glasses*, 1st ed. New York: Springer, 2008. [Online]. Available: https://epdf.pub/bulk-metallic-glasses-an-overview.html

[9]		Gottstein, *Physikalische Grundlagen der Materialkunde*, 4th ed. Berlin Heidelberg: Springer, 2014. doi: 10.1007/978-3-540-71105-6.

[10]		Yamaura, Zhang, and Inoue, *Novel Structured Metallic and Inorganic Materials*, 1st ed. Singapore: Springer, 2019. doi: 10.1007/978-981-13-7611-5.

[11]		Yue, Inoue, Liu, and Fan, "The development of structure model in metallic glasses," *Mater. Res.*, vol. 20, no. 2, pp. 326–338, 2017, doi: 10.1590/1980-5373-MR-2016-0318.

[12]		Ghidelli, "Size dependent mechanical behavior of Zr-Ni thin metallic glass films," PhD Thesis, Université catholique de Louvain, 2016.

[13]		Bernal, "A geometrical approach to the structure of liquids," *Nature*, vol. 183, no. 4655, pp. 141–147, 1959.

[14]		Cargill, "Dense random packing of hard spheres as a structural model for noncrystalline metallic solids," *J. Appl. Phys.*, vol. 41, no. 5, pp. 2248–2250, 1970, doi: 10.1063/1.1659198.

[15]		Polk, "The structure of glassy metallic alloys," *Acta Metall.*, vol. 20, no. 4, pp. 485–491, 1972, doi: 10.1016/0001-6160(72)90003-X.

[16]		Turnbull and Cohen, "Free-volume model of the amorphous phase: Glass transition," *J. Chem. Phys.*, vol. 34, no. 1, pp. 120–125, 1961, doi: 10.1063/1.1731549.

[17]		Rätzke and Faupel, "Diffusion in metallic glasses and undercooled metallic melts," *Zeitschrift fuer Met. Res. Adv. Tech.*, vol. 95, no. 10, pp. 956–960, 2004, doi: 10.3139/146.018046.

[18]		Miracle, "A structural model for metallic glasses," *Nat. Mater.*, vol. 3, no. 10, pp. 697–702, 2004, doi: 10.1038/nmat1219.

[19]		Fan, Liaw, Wilson, Dmowski, Choo, Liu, Richardson, and Proffen, "Structural model for bulk amorphous alloys," *Appl. Phys. Lett.*, vol. 89, no. 11, pp. 2004–2007, 2006, doi:

10.1063/1.2345276.

[20]   Fan, Liu, Chen, and Liaw, "Quantitatively defining free-volume, interconnecting-zone and cluster in metallic glasses," *Intermetallics*, vol. 57, pp. 98–100, 2015, doi: 10.1016/j.intermet.2014.10.008.

[21]   Inoue and Takeuchi, "Recent development and application products of bulk glassy alloys," *Acta Mater.*, vol. 59, no. 6, pp. 2243–2267, 2011, doi: 10.1016/j.actamat.2010.11.027.

[22]   Gu, Yang, Zhang, Shao, Zhao, and Yao, "Centimeter-sized Ti-rich bulk metallic glasses with superior specific strength and corrosion resistance," *J. Non. Cryst. Solids*, vol. 512, no. August 2018, pp. 206–210, 2019, doi: 10.1016/j.jnoncrysol.2018.10.034.

[23]   Schuh, Hufnagel, and Ramamurty, "Mechanical behavior of amorphous alloys," *Acta Mater.*, vol. 55, no. 12, pp. 4067–4109, 2007, doi: 10.1016/j.actamat.2007.01.052.

[24]   Şopu, Stukowski, Stoica, and Scudino, "Atomic-Level Processes of Shear Band Nucleation in Metallic Glasses," *Phys. Rev. Lett.*, vol. 119, no. 19, pp. 1–5, 2017, doi: 10.1103/PhysRevLett.119.195503.

[25]   Guo, Yan, Wang, Tan, Zhang, Sui, and Ma, "Tensile ductility and necking of metallic glass," *Nat. Mater.*, vol. 6, no. 10, pp. 735–739, 2007, doi: 10.1038/nmat1984.

[26]   Agrawal and Raj, "Measurement of the ultimate shear strength of a metal-ceramic interface," *Acta Metall.*, vol. 37, no. 4, pp. 1265–1270, 1989, doi: 10.1016/0001-6160(89)90120-X.

[27]   Glushko, Mühlbacher, Gammer, Cordill, Mitterer, and Eckert, "Exceptional fracture resistance of ultrathin metallic glass films due to an intrinsic size effect," *Sci. Rep.*, vol. 9, no. 1, pp. 1–9, 2019, doi: 10.1038/s41598-019-44384-z.

[28]   Li and Li, "Assessing the critical sizes for shear band formation in metallic glasses from molecular dynamics simulation," *Appl. Phys. Lett.*, vol. 91, no. 23, pp. 13–16, 2007, doi: 10.1063/1.2821832.

[29]   Wang, Fujita, Chen, Nieh, Okada, Koyama, Zhang, and Inoue, "Electrical conductivity of a bulk metallic glass composite," *Appl. Phys. Lett.*, vol. 91, no. 15, pp. 89–92, 2007, doi: 10.1063/1.2795800.

[30]   Liu, Hata, Wada, and Shimokohbe, "Thermal, mechanical and electrical properties of Pd-based thin-film metallic glass," *Japanese J. Appl. Physics, Part 1 Regul. Pap. Short Notes Rev. Pap.*, vol. 40, no. 9 A, pp. 5382–5388, 2001, doi: 10.1143/jjap.40.5382.

[31]   Gall, "Electron mean free path in elemental metals," *J. Appl. Phys.*, vol. 119, no. 8, 2016, doi: 10.1063/1.4942216.

[32]   Sun, Yao, Warren, Barmak, Toney, Peale, and Coffey, "Dominant role of grain boundary scattering in the resistivity of nanometric Cu films," *Phys. Rev. B - Condens. Matter Mater. Phys.*, vol. 79, no. 4, pp. 1–4, 2009, doi: 10.1103/PhysRevB.79.041402.

[33]   Gaganidze and Esquinazi, "Electron mean free path independence of the glasslike properties of polycrystalline metals," *J. Phys. IV JP*, vol. 6, no. 8, pp. C8-515-C8-518, 1996, doi: 10.1051/jp4:19968111.

[34]   Klement, Willens, Pol, and DUWEZ, "Non-crystalline Structure in Solidified Gold-Silicon Alloys," *Nature*, vol. 187, no. 4740, pp. 869–870, 1960, doi: http://dx.doi.org/10.1038/187869b0.

[35]   Schroers, Lohwongwatana, Johnson, and Peker, "Gold based bulk metallic glass," *Appl. Phys. Lett.*, vol. 87, no. 6, pp. 1–4, 2005, doi: 10.1063/1.2008374.

[36]   Guo, Zhang, Chen, Saotome, Fukuhara, and Inoue, "Effect of Au content on thermal stability and mechanical properties of Au-Cu-Ag-Si bulk metallic glasses," *Metall. Mater. Trans. A*, vol. 42, no. 6, pp. 1486–1490, 2011, doi: 10.1007/s11661-010-0584-9.

[37]   Matsuura, Zhang, Yamaura, Fujita, Ohara, Kohara, and Mizuno, "Structural features of the extraordinary low glass transition temperature for Au65Cu18Si17 bulk metallic glass," *Mater. Trans.*, vol. 54, no. 8, pp. 1351–1355, 2013, doi: 10.2320/matertrans.MF201307.

[38]   Chu, Huang, Jang, Wang, and Liaw, "Thin film metallic glasses: Preparations, properties, and applications," *Jom*, vol. 62, no. 4. pp. 19–24, 2010. doi: 10.1007/s11837-010-0053-3.

[39]   Seshan and Schepsis, *Handbook of Thin Film Deposition*, vol. 4, no. 1. Chennai: William Andrew, 2018.

[40]   Mattox, *Handbook of Physical Vapor Deposition (PVD) Processing*, 2nd ed. Oxford: William Andrew,   2010.   [Online].   Available: http://www.elsevier.com/wps/find/bookdescription.cws_home/717814/description#description

[41]   Kelly and Arnell, "Magnetron sputtering: A review of recent developments and applications," *Vacuum*, vol. 56, no. 3, pp. 159–172, 2000, doi: 10.1016/S0042-207X(99)00189-X.

[42]   Sarkar, *Sputtering Materials for VLSI and Thin Film Devices*, 1st ed. Oxford: William Andrew, 2014.

[43]   Fager, "Growth and Characterization of Amorphous TiAlSiN and HfAlSiN Thin Films," PhD Thesis, Linköping Studies in Science and Technology, 2014.

[44]   Thornton, "Influence of Apparatus Geometry and Deposition Conditions on the Structure and Topography of Thick Sputtered Coatings.," *J Vac Sci Technol*, vol. 11, no. 4, pp. 666–670, 1974, doi: 10.1116/1.1312732.

[45]   Ali, "Growth, transport, and magnetic properties of oblique-angle-deposited permalloy thin films," PhD thesis, Miami University, 2018.

[46]   Pauw, "A method of measuring specific resistivity and hall effect of discs of arbitrary shape," *Philips Res. Reports*, vol. 13, no. 1, pp. 1–9, 1958.

[47]   Limbu, "Developing a Novel Approach for Layer Controlled Graphene Synthesis and Tailoring the Properties for Applications," no. August, 2017, doi: 10.13140/RG.2.2.26125.18407.

[48]   Glushko, Klug, List-Kratochvil, and Cordill, "Monotonic and cyclic mechanical reliability of metallization lines on polymer substrates," *J. Mater. Res.*, vol. 32, no. 9, pp. 1760–1769, 2017, doi: 10.1557/jmr.2017.121.

[49]   Vegard, "The Structure of Silver Crystals," *Philos. Mag.*, vol. 31, pp. 111–169, 1916.

[50]   Swanson and Tatge, "Standard X-ray Diffraction Powder Patterns," *Natl Bur. Stand. (U.S.), Circ. 539*, vol. 1, p. 33, 1953.

[51]   Okamoto and Massalski, "The Au-Si (Gold-Silicon) system," *Bull. Alloy Phase Diagrams*, vol. 4, no. 2, pp. 190–198, 1983, doi: 10.1007/BF02884878.

[52]   Li, Zhao, Zhang, and Wang, "CaLi-based bulk metallic glasses with multiple superior properties," *Appl. Phys. Lett.*, vol. 93, no. 17, pp. 98–101, 2008, doi: 10.1063/1.2998262.

[53]   Faber and Ziman, "A theory of the electrical properties of liquid metals," *Philos. Mag.*, vol. 11, no. 109, pp. 153–173, 1965, doi: 10.1080/14786436508211931.

[54]   Ciuchi, Di Sante, Dobrosavljević, and Fratini, "The origin of Mooij correlations in disordered

metals," *npj Quantum Mater.*, vol. 3, no. 1, pp. 1–6, 2018, doi: 10.1038/s41535-018-0119-y.

[55] Cormier, Thomann, Dolique, Balhamri, Dussart, Semmar, Lecas, Brault, Snyders, and Konstantinidis, "IR emission from the target during plasma magnetron sputter deposition," *Thin Solid Films*, vol. 545, pp. 44–49, 2013, doi: 10.1016/j.tsf.2013.07.025.

[56] Jörg, Cordill, Franz, Kirchlechner, Többens, Winkler, and Mitterer, "Thickness dependence of the electro-mechanical response of sputter-deposited Mo thin films on polyimide: Insights from in situ synchrotron diffraction tensile tests," *Mater. Sci. Eng. A*, vol. 697, pp. 17–23, 2017, doi: 10.1016/j.msea.2017.04.101.

[57] Chu, Jang, Huang, Chou, Yang, Ye, Wang, Lee, Liu, Liaw, Chen, Lee, Li, and Rullyani, "Thin film metallic glasses: Unique properties and potential applications," *Thin Solid Films*, vol. 520, no. 16, pp. 5097–5122, 2012, doi: 10.1016/j.tsf.2012.03.092.

[58] Magagnosc, Feng, Yu, Cheng, and Gianola, "Isochemical control over structural state and mechanical properties in Pd-based metallic glass by sputter deposition at elevated temperatures," *APL Mater.*, vol. 4, no. 8, pp. 1–8, 2016, doi: 10.1063/1.4960388.

[59] Barna and Adamik, "Fundamental structure forming phenomena of polycrystalline films and the structure zone models," *Thin Solid Films*, vol. 317, no. 1, pp. 27–33, Apr. 1998, doi: 10.1016/S0040-6090(97)00503-8.

[60] Miccoli, Edler, Pfnür, and Tegenkamp, "The 100th anniversary of the four-point probe technique: The role of probe geometries in isotropic and anisotropic systems," *J. Phys. Condens. Matter*, vol. 27, no. 22, pp. 1–29, 2015, doi: 10.1088/0953-8984/27/22/223201.

[61] Glushko and Cordill, "Electrical Resistance of Metal Films on Polymer Substrates Under Tension," *Exp. Tech.*, vol. 40, no. 1, pp. 303–310, 2016, doi: 10.1007/s40799-016-0040-x.

[62] Kutschej, Mitterer, Mulligan, and Gall, "High-temperature tribological behavior of Cr'N-Ag self-lubricating coatings," *Adv. Eng. Mater.*, vol. 8, no. 11, pp. 1125–1129, 2006, doi: 10.1002/adem.200600131.